Catalytic Resonance Theory:
SuperVolcanoes, Catalytic Molecular Pumps,
and Oscillatory Steady State

M. Alexander Ardagh[1,2], Turan Birol[1], Qi Zhang[1],
Omar Abdelrahman[2,3], Paul J. Dauenhauer[1,2*]

[1]University of Minnesota, Department of Chemical Engineering and Materials Science, 421 Washington Ave SE, Minneapolis, MN 55455
[2]Catalysis Center for Energy Innovation, University of Delaware, 150 Academy Street, Newark, DE 19716
[3]University of Massachusetts Amherst, Department of Chemical Engineering, 159 Goessmann Laboratory, 686 North Pleasant Street, Amherst, MA 01003.
*Corresponding author: hauer@umn.edu

Abstract. Catalytic reactions on surfaces with forced oscillations in physical or electronic properties undergo controlled acceleration consistent with the selected parameters of frequency, amplitude, and external stimulus waveform. In this work, the general reaction of reversible A-to-B chemistry is simulated by varying the catalytic (heat of reaction, transition state and intermediate energies) and oscillation parameters (frequency, amplitude, endpoints, and waveform) to evaluate the influence on the overall catalytic turnover frequency and steady state extent of conversion. Variations of catalytic cycle energies are shown to comprise a superVolcano of superimposed individual Balandin-Sabatier volcano plots, with variations in linear scaling relationships leading to unique turnover frequency response to forced oscillation of the catalyst surface. Optimization of catalytic conditions identified a band of forced oscillation frequencies leading to resonance and rate enhancement as high as 10,000x above the static Sabatier maximum. Dynamic catalytic reactions conducted at long times achieved oscillatory steady state differing from equilibrium consistent with the imposed surface oscillation amplitude acting as a 'catalytic pump' relative to the Gibbs free energy of reaction.

1.0 Introduction. The efficient catalytic transformation of feedstocks to chemicals and materials for society remains at the forefront of technological needs in the 21st century.[1] Grand challenges in catalysis aim for the sustainable manufacture of monomers[2,3,4], the elimination of carbon dioxide[5,6], the fixing of nitrogen[7,8,9,10], and the environmental remediation of pollutants[11,12]. New catalysts should be synthesized from low-cost, earth-abundant materials[13] that operate with long-term stability and negligible environmental impact within a process designed to optimally benefit from catalytic rate enhancement. Catalyst development also aims for maximum catalytic rate within the limitations of the Sabatier principle[14] for multi-step chemistry which includes adsorption, surface catalytic reactions, and desorption (Figure 1A).

Catalyst design has historically focused on selecting the optimum catalytic active site within a material which provides a balance of strong and weak adsorbate binding energies[15]. Strong binding is rate limiting in desorption resulting in rate inhibition from the product, while weak binding is limiting in dissociative adsorption or surface reaction[16,17,18]. The original strategy in these systems tuned catalyst characteristics to exist at the maximum possible turnover frequency (i.e., the Sabatier volcano peak)[19]. More recent strategies aim to shift the volcano peak via alteration of the linear scaling relations, which describe the predicted surface activation energy as a function of surface reaction enthalpy[20,21,22,23]. Varying of the linear scaling relations of surface reaction activation energies has the potential to
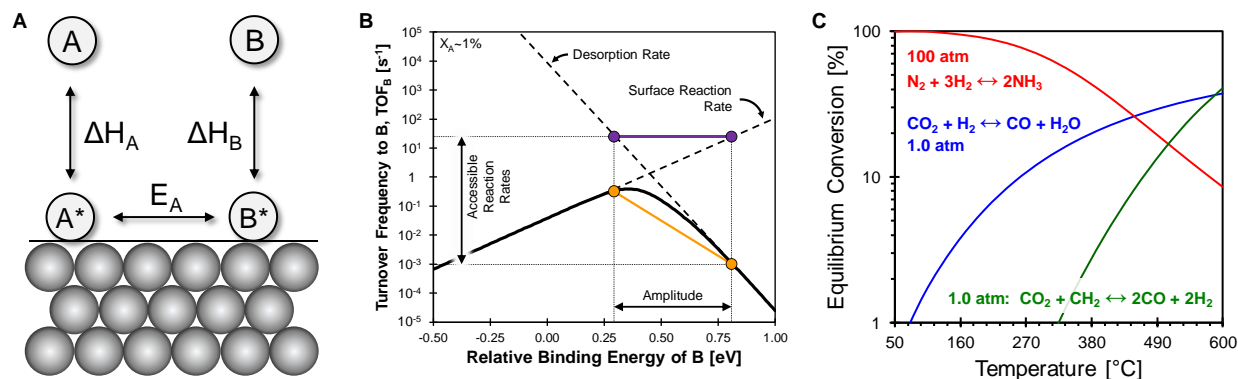
Figure 1. Kinetic and Thermodynamic Challenges of Catalytic Reactions. (A) Gas-phase chemical species A and B react on catalyst surfaces through adsorbed surface species A* and B* with forward activation energy, E_a. **(B)** Conversion of A-to-B general chemicals volcano curve operating at 1% conversion with oscillating binding energy of B* with resonance rate in purple. **(C)** Reaction equilibrium of ammonia synthesis (red), reverse water-gas-shift (blue), and dry reforming of methane (green).

change the shape of Sabatier volcano plots and shift the maximum possible turnover frequency.

We have recently described an alternative concept for catalyst enhancement in the form of surface adsorbate binding oscillation[24]. By this approach depicted in Figure 1B, the catalyst surface undergoes periodic external stimulation (e.g. electric field, strain) such that reaction surface intermediates experience oscillating binding energy with time. The amplitude of the oscillating stimulus generates variation in surface species binding energy, with the endpoints of the oscillation amplitude dictated by the combination of the selected catalyst surface and the condition of the external stimulus. Stimulus waveforms can also vary in frequency, type (e.g. square, sinusoidal), and periodicity (e.g. combinations of waveforms). For the reversible A to B reaction, the highest catalytic turnover frequency occurs over a band of imposed frequencies which resonate with the natural frequencies of the catalytic surface reaction.

The turnover frequency response of the catalytic system to external oscillating stimuli depends on the kinetics of the surface mechanism and the resulting shape of the Balandin-Sabatier volcano curve[25,26]. A catalytic system may exhibit a linear Brønsted-Evans Polanyi (BEP) relationship with slope, α, and intercept, β, relating the surface reaction thermodynamics to the surface reaction transition state. However, another consideration in volcano plot architecture is the dynamic response of individual surface species (e.g., A*, B*) to external stimulus. For variation of any descriptor (e.g. binding energy of an intermediate or single

atom), surface species exhibit differing binding energies with the surface. In our previous work on surface resonance of the reversible A to B reaction[24], the considered catalytic system exhibited two-fold variation in the binding energy of B* relative to A* for the same extent of external stimulus. A broader understanding of this ratio (referred to here as gamma, γ) on the structure of volcano plots is required to predict the potential of imposed external dynamic stimulus across a broad range of catalytic chemistries and materials.

In addition to rate, chemical equilibrium between the reactants and products limits many catalytic systems. As shown in Figure 1C, industrially important reactions including ammonia synthesis, water-gas shift chemistry, dry reforming of methane, methanol synthesis, and alkane dehydrogenation all exhibit Gibbs free energy of reaction (and associated equilibrium constants, K_i) at standard conditions limiting high overall conversion[27,28,29,30,31]. To overcome these inherent limitations, equilibrium between reactants and products can be manipulated via reaction conditions; ammonia synthesis is operated at high pressure[32,33], while water-gas-shift chemistry is conducted in staged reactors of varying temperature[34,35]. Other strategies for overcoming equilibrium limitations combine a second reaction or separation phenomenon to drive a reaction. For example, alkane dehydrogenation is combined with oxidation[36], ammonia synthesis is combined with absorption[37,38], and carbon-carbon coupling chemistries such as cycloaddition can be combined with dehydration[39,40].

The driving force for chemical reaction is the difference in Gibbs free energy between reactant and product, with a reaction system stabilizing at equilibrium defined as the two states existing at equal Gibbs free energy. The two strategies for manipulating reactions are based on this definition; change the conditions and equilibrium, or deprive the system of one of the two components (reactant or product) to unbalance the free energy distribution (i.e., Le Chatelier's principle)[41,42]. A third strategy for driving physical systems away from equilibrium is the application of work; added energy can perturb a physical system to a steady-state condition different from equilibrium such as the case of electrocatalytic water splitting[43,44] or electrocatalytic ammonia synthesis[45]. Alternatively, a catalyst surface with dynamically-oscillating adsorbate binding energy provides work to a catalytic reaction to raise the energy of adsorbed surface species[46]. The imposed amplitude of surface binding energy oscillation ($0.1 < \Delta U < 1.5$ eV) serves as a 'catalytic pump' to raise a surface adsorbate to a higher energy state. This surface energy input manifests as a rate enhancement and a deviation from equilibrium of the surface reaction, with the extent of variation in reaction rate and conversion depending on the type of catalytic chemistry as well as the parameters associated with the imposed oscillating surface stimulus.

Here we will map out the different structures of Sabatier volcano plots based on definitions of the five key parameters of single-reaction (A-to-B) reversible catalytic systems. Example systems representative of the different kinetic regimes associated with different kinetic parameter combinations are simulated as catalytic reactors to explore the ability of the dynamically oscillating catalyst surface to preferentially promote catalytic turnover frequency. Selected systems are evaluated within the context of the forced oscillator parameters of imposed surface binding energy frequency, amplitude, amplitude position, and oscillating waveform. Specific conditions are identified leading to surface resonance and enhanced overall catalytic rate relative to the Sabatier maximum, while other conditions preferentially promote a steady state condition differing from equilibrium. The relationship between the applied oscillation energy (i.e., surface work) and the resulting oscillatory steady state is then evaluated to understand the conditions leading to tunable reaction conversion with broad application.

2.0 Computational Methods. Computational simulations were conducted using Matlab 2017b and 2019a, as well as the supercomputing resources at the Minnesota Supercomputing Institute (MSI). Reactor and dynamic catalysis codes are provided in SI section S1. A model reversible reaction (A ↔ B) was implemented as a gas-phase catalytic reaction system with three reversible elementary steps: (i) reversible adsorption of A, (ii) surface forward and reverse reaction of A* ↔ B*, and (iii) reversible desorption of B. Pre-exponential factors were set to constant values typical for each type of elementary step. For adsorption steps, a pre-exponential of 10^6 (bar-s)$^{-1}$ was selected, while a pre-exponential of 10^{13} s^{-1} was used for surface reaction and desorption steps. Surface reaction activation energies ($E_{a,sr}$) were calculated based on the specified Brønsted-Evans-Polanyi (BEP) relationship parameters and the heat of reaction for the surface reaction (ΔH_{sr})[47], as shown in Equation 1. The activation energy of adsorption was set to 0 kJ mol^{-1}, and the activation energy of desorption was set to the binding energy for each species,

$$E_{a,sr} = \alpha \Delta H_{sr} + \beta \qquad (1)$$

where α is the BEP proportionality constant, and β is the BEP offset.

The reaction chemistry was specified by the overall gas-phase heat of reaction (ΔH_{ovr}), species binding energies (BE_A and BE_B), and the BEP relationship parameters (α and β). Vapor-phase flow reactors (CSTR) and batch reactors were modeled by systems of ordinary differential equations (ODEs) with two gas phase species, A and B, and two surface species, A*, B*, with open site *. Differential equations for the CSTR were as follows:

$$\frac{d[A]}{dt} = \frac{\dot{q}}{V}([A]_f - [A]) - k_{1,f}[A]RT\theta^* \frac{N_{sites}}{V} + k_{1,r}\theta_A^* \frac{N_{sites}}{V} \qquad (2)$$

$$\frac{d[B]}{dt} = \frac{\dot{q}}{V}([B]_f - [B]) - k_{3,r}[B]RT\theta^* \frac{N_{sites}}{V} + k_{3,f}\theta_B^* \frac{N_{sites}}{V} \qquad (3)$$

$$\frac{d\theta_A^*}{dt} = k_{1,f}[A]RT\theta^* - k_{1,r}\theta_A^* - k_{2,f}\theta_A^* + k_{2,r}\theta_B^* \quad (4)$$

$$\frac{d\theta_B^*}{dt} = k_{3,r}[B]RT\theta^* - k_{3,f}\theta_B^* + k_{2,f}\theta_A^* - k_{2,r}\theta_B^* \quad (5)$$

where [A] and [B] are gas phase concentrations in M, $\dot{q}$ is the volumetric flow rate in liters/s, V is the reactor bed volume in liters, k's are rate constants in (bar-s)$^{-1}$ or s^{-1}, θ's are surface coverages, and N_{sites} is the number of catalytic active sites. In addition, surface coverage is constrained by the site balance shown in Equation 6.

$$1.0 = \theta^* + \theta_A^* + \theta_B^* \quad (6)$$

For batch reactors, the flowrate terms from Equations 2 and 3 are removed.

Differential equations were solved using built-in Matlab ODE solvers ODE15s and ODE23tb along with the "Radau" 3rd party Matlab ODE solver. Tight solver tolerances of 10^{-6}-10^{-8} relative tolerance and 10^{-9} absolute tolerance were used due to the ultra-stiff nature of the static and dynamic catalysis systems. Performance comparison of the various Matlab ODE solvers can be found in SI section S2. Computational times were measured using the 'tic' and 'toc' commands which act as a stopwatch timer. The stopwatch was initiated right before dynamic catalysis was applied in a simulation and stopped after the last dynamic catalysis iteration.

Dynamic catalysis was implemented by varying the binding energies of A and B using square, sinusoidal, triangle, and sawtooth shaped

waveforms. Waveforms were defined by their oscillation amplitude ΔU in electron volts (eV), oscillation frequency f in hertz (Hz), and oscillation endpoints in eV. Oscillation amplitude is noted relative to either surface intermediate as ΔU_A or ΔU_B. The binding energies of A and B were varied using a defined proportionality constant, γ, according to Equation 7,

$$\Delta BE_B = \gamma \Delta BE_A \quad (7)$$

where the change in the binding energy of B was specified using one of the four different waveform equations (e.g. sinusoidal). A second parameter, δ, was defined for the relationship between binding energies. At any binding energy of B, the binding energy of A was calculated using Equation 8:

$$BE_A = (BE_B - (1 - \gamma)\delta - \Delta H_{ovr})/\gamma \quad (8)$$

Heat maps of catalytic turnover frequency to B (TOF$_B$) were created in Matlab 2019a by interpolating over discrete data sets obtained at varying oscillation amplitudes, oscillation frequencies, and oscillation endpoints. The modified Akima cubic Hermite or spline interpolation method was used to fit data sets and the 'smoothdata' function was employed with the moving average or Savitzky-Golay filter method to average out overshoots due to interpolation. Complete tabulated data sets of all heat maps are provided in the supporting information.

3.0 Results and Discussion. As shown in Figure 2A, a general reaction enthalpy diagram for chemical species A reversibly converting to B forms intermediates A* and B* with transition
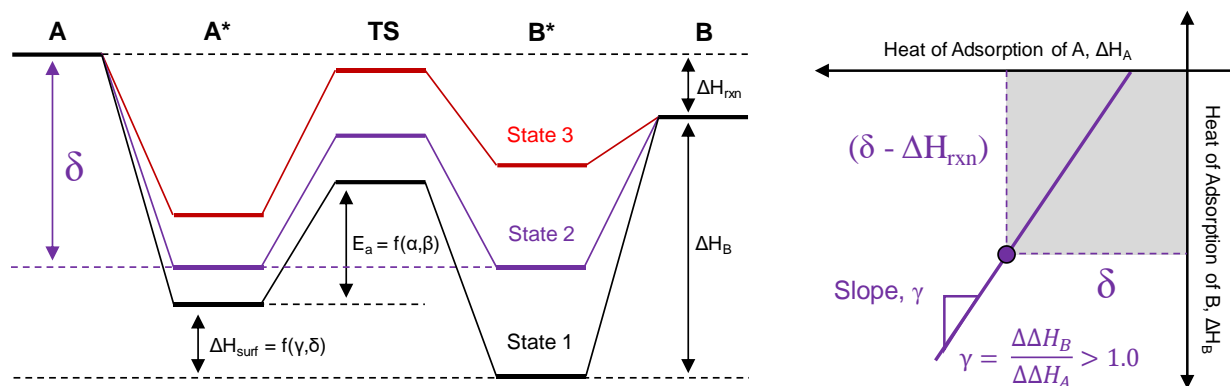
Figure 2. Parameters of Dynamic Heterogeneous Catalysis. **Left.** State-energy diagram of oscillating heterogeneous catalyst. **Right.** Variation of the binding energy of B* linearly scales with the binding energy of A* with slope, γ_{B-A}, and common point, δ.

state, TS, in between. The overall heat of reaction, ΔH_{ovr}, remains fixed for all conditions of catalyst surface dynamics. Two more variables are required to define the transition state (TS) energy, E_a, which will vary with the surface intermediate energies. As stated in Equation 1, the existing BEP relationships with slope, α, and intercept, β, fully define all possible transition state energies for catalytic systems exhibiting this linear relationship.

Two new variables are required to define the variation of surface intermediate energies. Due to the differences in electronic and steric interactions with the surface, variation of surface adsorbate binding energies with external stimuli will not affect all surface adsorbates equally. As depicted in Figure 2A, the binding energy of A* changes less than B* between each of the three potential states resulting from external stimulus. To describe this change differential, the extent of change is defined to be gamma equal to the difference in binding energy of B* divided by the difference in binding energy of A*,

$$\gamma_{B-A} = \frac{\Delta\Delta H_B}{\Delta\Delta H_A} \qquad (9)$$

Additionally, there exists one condition (purple in Figure 2A) leading to A* and B* existing at the same surface energy; that energy is identified in Figure 2A as delta, δ [eV].

If the external stimulus of a catalytic surface imposes a linear response in the binding energy of the surface adsorbates, then potential dynamic catalysis scenarios can be depicted in the right panel of Figure 2B. As shown, the binding enthalpies of A* and B* are related by a line with slope, gamma γ_{B-A}. It is important to note that gamma is defined, and consideration of the reaction in reverse will produce a gamma of inverse value. The point of common surface energy, delta δ, exists for the enthalpy of adsorption of B offset by the heat of reaction. More complicated relationships (i.e., non-linear) between the surface energies of intermediate species require more than two variables, depending on the applied model.
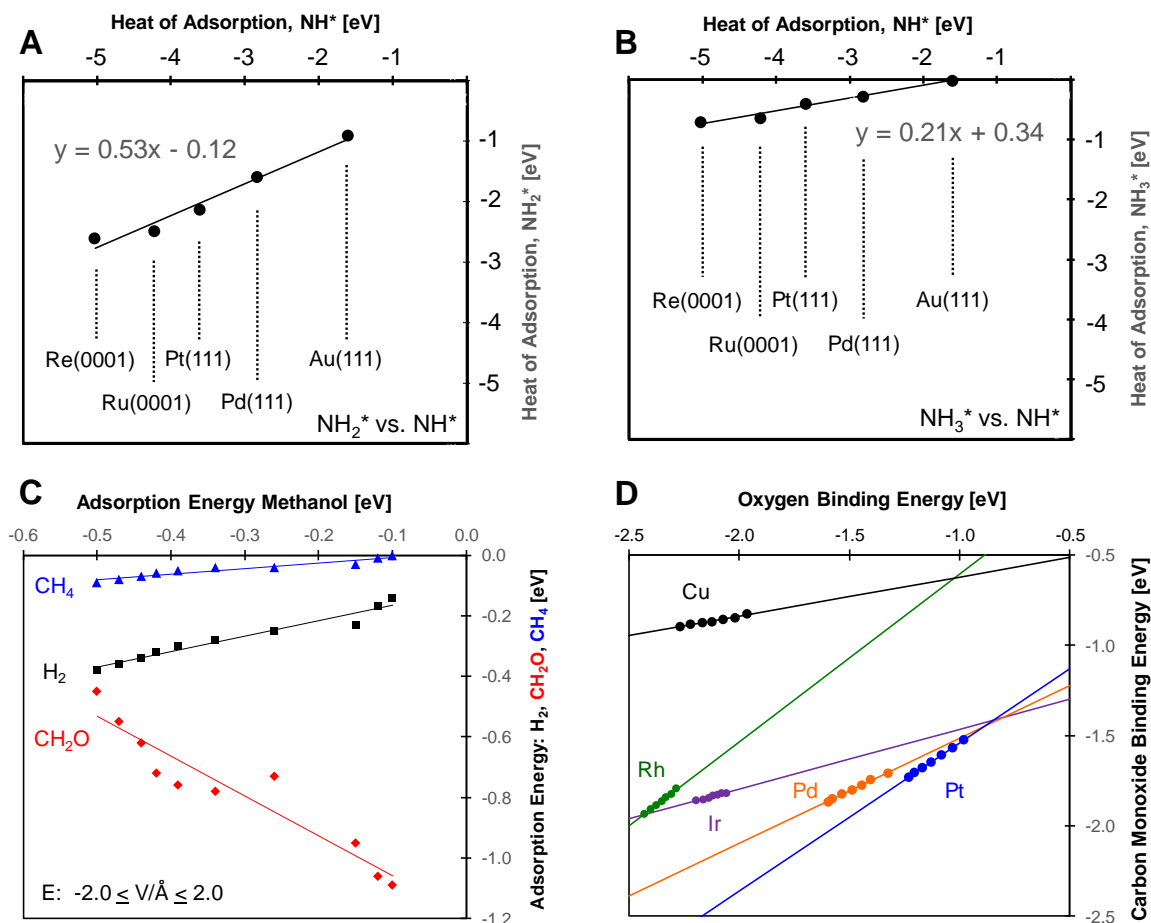
3.1 External Catalytic Stimuli. The ability to tune adsorption enthalpy (also referred to as binding energy, $BE = -\Delta H_{ads}$), requires external stimulus to modify the catalyst, adsorbate, or interacting surface bond. One method of catalyst stimulus is surface strain, which has been shown in static systems (e.g., films on lattice-mismatched

substrates) to shift the metal *d*-band center and alter the adsorption enthalpy of surface adsorbates[48,49,50,51]. Electric fields applied to adsorbed species can also tune the binding energy of adsorbates with benefits for controlling and accelerating catalytic surface chemistry, including externally imposed fields or internal fields arising in electrocatalytic reactors[52,53,54]. Other strategies aim to alter the electronic structure of surface metal atoms, such as field-effect modulation with a dielectric and imposed back gate-voltage; this method moves charge carriers into the surface catalyst layer (e.g. metal or metal oxide) to shift the *d*-band center and ultimately the interaction with surface adsorbates[55,56, 57,58]. The impact of these techniques on the relative changes in surface intermediate energies and variation in the gamma-delta plot (e.g., Figure 2B) of two surface adsorbates depends with each combination of surface intermediates, surface material/facet, and type of imposed stimulus which so far has been primarily explored via computation.

An initial comparison across surface intermediate binding energies can be made by comparing the energies between metals and metal surface planes. For the case of ammonia, the surface adsorption enthalpy of N*, NH*, NH$_2$*, and NH$_3$* have been calculated by Mavrikakis and co-workers on Re(0001)[59], Ru(0001)[60], Pt(111)[61], Pd(111)[62], and Au(111)[63]. As shown in Figure 3A and 3B, the adsorption enthalpies of the various intermediates are plotted relative to one another with the gamma values of the intermediates apparent in the fitted linear slopes. In the comparison of NH* and NH$_2$*, the binding energy of NH* changes almost twice as much as the binding energy of NH$_2$* (slope ~ γ_{NH2-NH} ~ 0.53). Similarly, in the comparison of NH* and NH$_3$*, the binding energy of NH* changes almost five times as much as the binding energy of NH$_3$* (γ_{NH3-NH} ~ 0.21). These comparisons exist across different metals, which is not a realistic scenario for implementing dynamic catalysis (i.e., metals cannot be periodically interchanged). Only external stimulus on a single catalyst surface is likely to physically achieve the conditions necessary for dynamic catalytic resonance and rate promotion.

Comparison of the potential for tuning adsorbate binding energy via external stimuli are presented for imposed electric field (Figure 3C) and

A Heat of Adsorption, NH* [eV]

B Heat of Adsorption, NH* [eV]

C Adsorption Energy Methanol [eV]

D Oxygen Binding Energy [eV]

Figure 3. Gamma Parameters of Ammonia Synthesis. (**A**) The heat of adsorption of NH* and NH$_2$* vary by γ ~ 0.53. (**B**) The heat of adsorption of NH* and NH$_3$* vary by γ ~ 0.21. Data for panels A and B calculated by Mavrikakis and co-workers[59-63]. (**C**) The heat of adsorption of methanol varies differently than methane (CH$_4$), hydrogen (H$_2$), and formaldehyde (CH$_2$O) on Ni metal in the presence of an electric field varying between -1.0 to +1.0 V/Å calculated by McEwen and co-workers[64]. (**D**) The binding energy of oxygen, O*, and carbon monoxide, CO*, on Copper (black), Rhodium (green), Iridium (purple), Palladium (orange), and Platinum (blue) with strain of -3.0% to +3.0%[65].

surface strain (Figure 3D). As calculated by McEwen and co-workers[64], electric fields ranging from -1.0 to +1.0 V/Å applied to a Nickel surface resulted in significant variation of the binding energy of methane (blue in Figure 3C), hydrogen (black), and formaldehyde (red) relative to methanol. From the slopes of a linear best fit, methane varied less with changes in methanol (slope ~ γ$_{CH4-CH3OH}$ ~ 0.18) than hydrogen (γ$_{H2-CH3OH}$ ~ 0.51), while formaldehyde actually decreased in binding energy as methanol increased in binding energy (γ$_{CH2O-CH3OH}$ ~ -1.31). Another method of varying surface binding energy of surface strain is presented in Figure 3D using the calculated binding energies of Shengchun Yang and co-workers[65]. As depicted in Figure 3D, the binding energy of carbon monoxide and atomic oxygen were calculated for

the lowest energy adsorption geometry on the M(111) surface of five different metals: Cu (black), Rh (green), Ir (purple), Pd (orange), and Pt (blue). Binding energies varied due to imposed surface strain of -3.0% to +3.0%; while this large surface strain is likely not physically feasible, it does provide insight into the relative impact of strain on oxygen relative to carbon monoxide. From these calculations, there exists some initial evidence that a two-parameter linear model can effectively describe the relative change in binding energy between two surface adsorbates.

3.2 Catalytic Dynamics - Definition. With the definition of parameters in Figure 2 and the calculations presented in Figure 3, it is possible to completely define the surface catalytic kinetics for a dynamic chemistry with five parameters: ΔH$_{ovr}$,
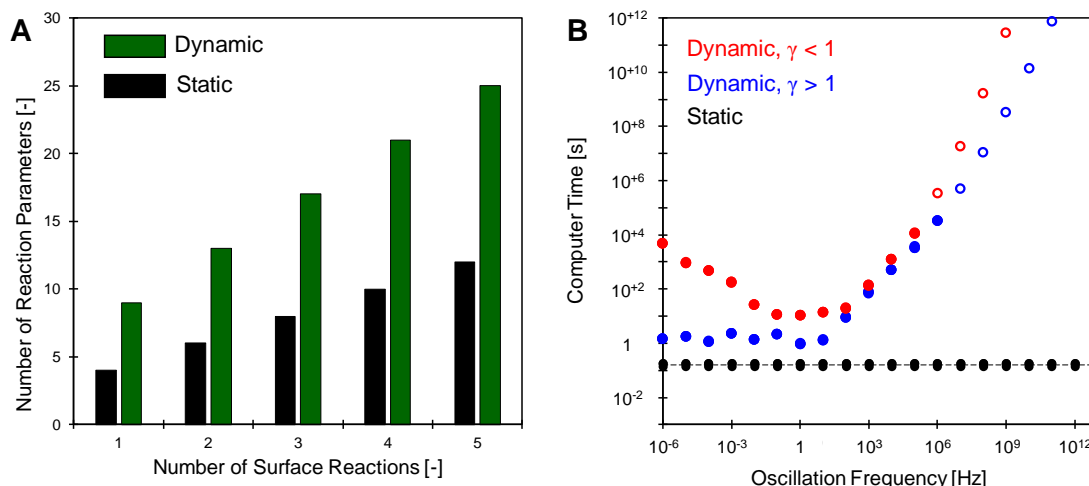
Figure 4. Reaction Parameters of Static and Dynamic Surface Mechanisms. (A) The number of parameters required to define all energies of all states in a catalytic surface reaction mechanism differ between a static, steady-state reaction and a dynamic catalytic reaction with oscillating states. Reactor parameters (e.g., temperature, pressure, composition, space time) are not included in this figure. **(B)** Computational time for static (black), dynamic ($\gamma_{B-A} <$ 1, red), and dynamic ($\gamma_{B-A} > 1$, blue) simulations; filled data points are determined from simulation, while open circles are determined by extrapolation. Conditions: CSTR, P of 100 bar, $\alpha \sim 0.6$, $\beta \sim 102$ kJ mol^{-1}, $\delta \sim 1.4$ eV, Yield of B of 1.0 %, f_{osc} varies, and $\Delta U_B \sim 0.6$ eV. For $\gamma_{B-A} < 1$: T of 100 °C, ΔH_{ovr} of 0 kJ mol^{-1}, and asymmetric oscillation endpoints. For $\gamma_{B-A} > 1$: T of 150 °C, ΔH_{ovr} of -20 kJ mol^{-1}, and symmetric oscillation endpoints.

α and β to define the activation energy linear scaling relationship, and γ and δ to define the linear adsorption energy scaling relationship. Four additional parameters exist related to the applied dynamics of the catalyst binding energy oscillation including: (1) surface oscillation frequency, f, (2) surface oscillation amplitude, ΔU, (3) surface oscillation endpoint, U_E, and (4) surface oscillation waveform shape (e.g., square, sinusoidal, etc.). Additional parameters are required if the applied surface stimulus is a composite of imposed oscillations each with their own frequency and amplitude. Finally, simulation of the dynamic catalyst system requires all of the parameters associated with the reactor including temperature, pressure, reactant composition, and space time.

The introduction of dynamics for the simple system of A reversibly reacting to B requires nine variables for definition, which is more than double the four parameters required to define the static catalytic reaction (two adsorption enthalpies, one activation energy, and overall reaction enthalpy). As depicted in Figure 4A, as the complexity of catalytic systems expands by the number of catalytic surface reactions, the number of parameters required to define the oscillating systems significantly expands. Dynamic systems require at least $2n + 1$ parameters to define all

energetic states, where n is the number of parameters required to define the static catalytic reaction. If the scaling relationships to predict changes in the transition state energy or the relative binding energies of surface intermediates become nonlinear, then the number of parameters further expands accordingly.

The time required to achieve steady state in a simulated continuous-flow stirred-tank reactor with a dynamically operating catalyst increases orders of magnitude from the simulation with a static catalyst. As depicted in Figure 4B, the considered A-to-B reversible catalytic reaction was simulated using Matlab to achieve steady-state reaction conditions in less than one second. However, introduction of dynamics immediately increased computational time to greater than a second for all conditions. In particular, computational time increased logarithmically above about 100 Hz such that simulations above megahertz-imposed catalyst binding energy waveforms required more than 10^4 seconds (~ 3.0 hrs).

Increased computational time is associated with the large number of oscillations required to achieve steady-state surface and reactor conditions. As depicted in Figure 5A, a catalytic batch reactor
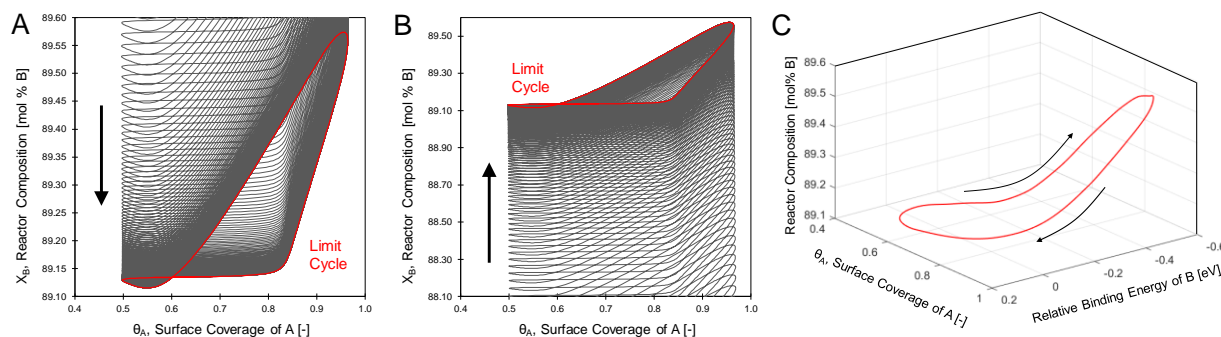
Figure 5. Dynamic Forced Oscillation of Surface Binding Energy – Limit Cycles. A simulated catalytic batch reactor reversibly converting A to B with oscillating binding energy of B* exhibits dynamic variation in surface coverage and gas-phase composition approaching a limit cycle. **(A)** Initial conditions above the limit cycle reactor composition, 95 mol% B. **(B)** Initial conditions below the limit cycle reactor composition, 10 mol% B. **(C)** The limit cycle consists of a three-dimensional stable loop with non-overlapping variations of binding energy of B*, surface coverage of A, and reactor composition. Catalytic conditions: $\alpha \sim 0.6$, $\beta \sim 130$ kJ mol^{-1}, $\gamma_{B-A} \sim 2.0$, $\delta \sim 1.4$ eV, $f \sim 1.0$ Hz, $\Delta U_B \sim 0.6$ eV, and $\Delta H_{rxn} \sim 0$ kJ/mol.

operating at long times with initially high concentrations of B (95 mol%) slowly decreases in concentration until achieving the steady state limit cycle (red). When starting from a low concentration of B (10 mol%), the composition slowly increases until achieving the same limit cycle (Figure 5B). This steady state solution (Figure 5C) varies in time in surface coverage and reactor composition, but the average composition is fixed in time. As is visually apparent, the composition approaches the limit cycle only minimally for each imposed binding energy cycle, requiring significant computational time to identify the solution for each parameter set of catalyst and oscillation conditions.

*3.3 Surface Parameters and SuperVolcanoes.* The large number of catalytic parameter combinations indicates the importance of categorizing general behaviors of Sabatier-principle-controlling catalytic reactions. One strongly-determining parameter is γ, the ratio of the extent of change of one surface species relative to another as defined in Equation 9. To understand the impact of γ on the catalytic reaction, all possible volcano plots are generated in Figure 6A for 17 variations ($0.3 \leq \gamma_{B-A} \leq 9.0$), while the surface coverages of A* and B* are depicted for low γ_{B-A} (Figure 6B-6C) and high γ_{B-A} (Figure 6D-6E). As shown, the change in γ_{B-A} from above and below unity dramatically alters the surface coverages and overall kinetics of the catalytic reaction system. However, by superimposing all rate volcano plots on the same panel (Figure 6A), it is apparent that

there exists global behavior; the entire superimposed set of possible volcano curves are bounded by a 'superVolcano' of extreme limits. All potential volcano curves are bounded at low binding energy of B* by the rate of adsorption, while high bending energy binds the overall rate of desorption. All variations from the superVolcano bounds result only from limitations arising from the surface reaction.

For catalytic systems with high γ_{B-A} (>1.0, blue), the surface product B* lowers in energy faster than A*, resulting in a decreasing transition state energy and activation energy by the linear scaling relationship; for this reason, high gamma systems exhibit an increasing turnover frequency with increased binding energy of B* consistent with a sharp volcano peak depicted in Figure 6A. In contrast, the low γ_{B-A} catalytic systems (γ <1.0, red) exhibit three regimes. At low binding energy (< -0.4 eV), the surface is bare, and the overall rate is controlled by the rate of adsorption; at moderate binding energies (-0.4 eV < BE$_B$ < 0.2 eV), the rate is controlled by desorption. Even higher binding energies lead to surface reaction control. The common point of all curves (0.2 eV relative binding energy of B*) is equal to the linear scaling parameter, $\delta \sim 1.4$ eV (offset relative to a binding energy of B of 1.0 eV).

The surface coverages of the volcano curves of Figure 6 shift with the binding energy of B* consistent with the rate-controlling phenomenon. At low BE$_B$, the surface is bare. For the high γ_{B-A} systems (blue, γ > 1.0), the surface becomes
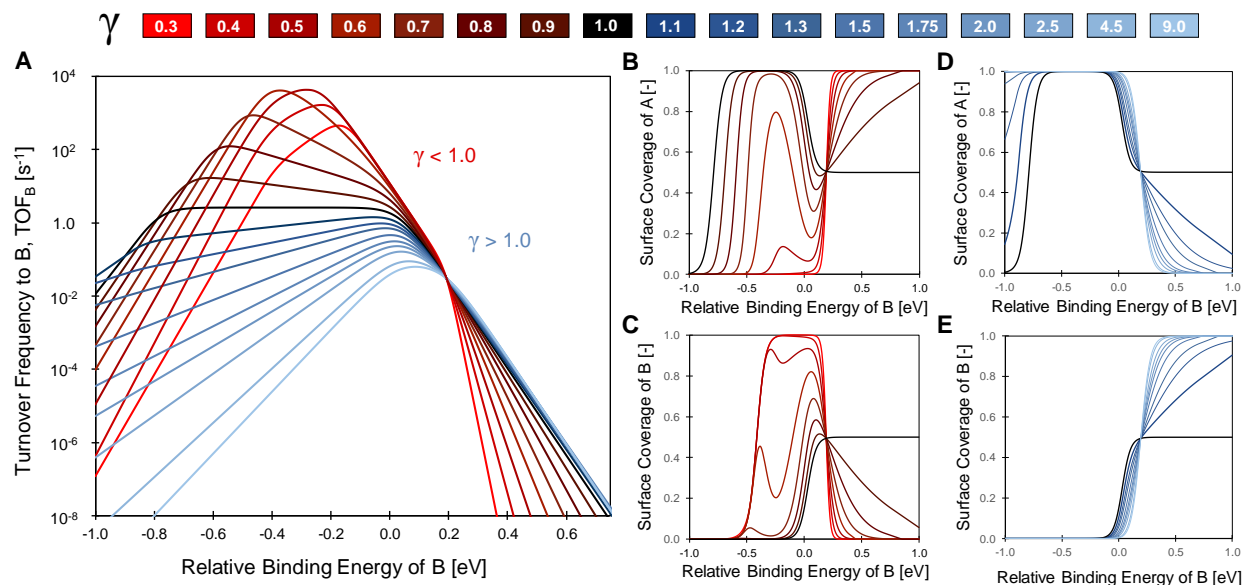
Figure 6. Balandin-Sabatier Volcano Curves for Varying γ-Parameter. (A) Turnover frequency to B product. **(B).** Surface coverage of A in low γ_{B-A} systems. **(C)** Surface coverage of B in low γ_{B-A} systems. **(D)** Surface coverage of A in high γ_{B-A} systems. **€.** Surface coverage of B in high γ_{B-A} systems. All panels – conditions: $Y_B \sim 1\%$, P ~ 100 bar, T ~ 150 °C, α ~ 0.6, β ~ 102 kJ mol^{-1}, and δ ~ 1.4 eV.

covered in A* as binding energy increases only to be completely replaced by B* at the transition point of +0.2 eV. The opposite behavior exists for low γ_{B-A} systems (red, γ < 1.0); the surface is covered in A* at high binding energy. The only variation is the transition observed between high and low surface coverage of A* and B* at moderate binding energies.

Four superVolcano plots were created to compare the impact of changing α, β, and δ on the superVolcano shapes and kinetic behaviors as shown in Figure 6A and Figure 7A-7C. The independent-axis for Figure 6A is zero when the binding energy of B is 1.0 eV, and the independent-axis zeros for Figure 7A, 7B and 7C are the corresponding delta values (0.3, 1.2, and 0.3 eV, respectively). In the first superVolcano in Figure 6A, low γ_{B-A} (< 1.0) systems had higher overall performance with a maximum TOF$_B$ of ~10^4 s^{-1} at relatively weak binding of A and B (0.6 eV for the binding energy of B). Low γ_{B-A} volcano plots exhibited three distinct regions with varying rate-limiting steps: (i) adsorption, (ii) surface reaction/adsorption, and (iii) desorption. Conversely, high gamma (γ > 1.0) volcano plots had two primary regions: (i) surface reaction limited and (ii) desorption-limited regimes. All volcano plots intersected at a single point,

corresponding to the equivalence point, where the binding energy of B is (δ + ΔH_{ovr}).

Figure 7A demonstrates the changes due to lowering the value of δ from 1.4 eV to 0.5 eV in comparison with Figure 6A. At low δ, the high γ_{B-A} curves have higher TOF performance across a wide span of binding energies, but the maximum TOF$_B$ is lowered to ~10^2 s^{-1}. In addition, the intermediate regime of the low γ_{B-A} plots moves to the right of the volcano plot peak at absolute binding energies of 0.5-1.3 eV, so there now exists a surface reaction/desorption limited regime. The high γ_{B-A} curves coalesce on the desorption limited line at ~1.3 eV and onwards in Figure 7A, meaning that these systems are nearly saturated with B* and the TOF$_B$ is solely dependent on the binding energy of B past this point.

Figure 7B depicts the superVolcano trend for lower β values as compared with Figure 6A; β was lowered to 65 kJ/gmol versus 102 kJ/gmol in Figure 6A. The high γ_{B-A} curves gain two new rate-limiting kinetic regimes, with adsorption limited behavior until an absolute binding energy of 0.4 eV, surface reaction/adsorption until 0.9 eV, surface reaction/adsorption from 0.9 eV to 1.4 eV, and desorption limited behavior from 1.4 eV onwards. As expected, the overall maximum TOF$_B$ increases to ~10^5 s^{-1} since a lower β allows for higher surface
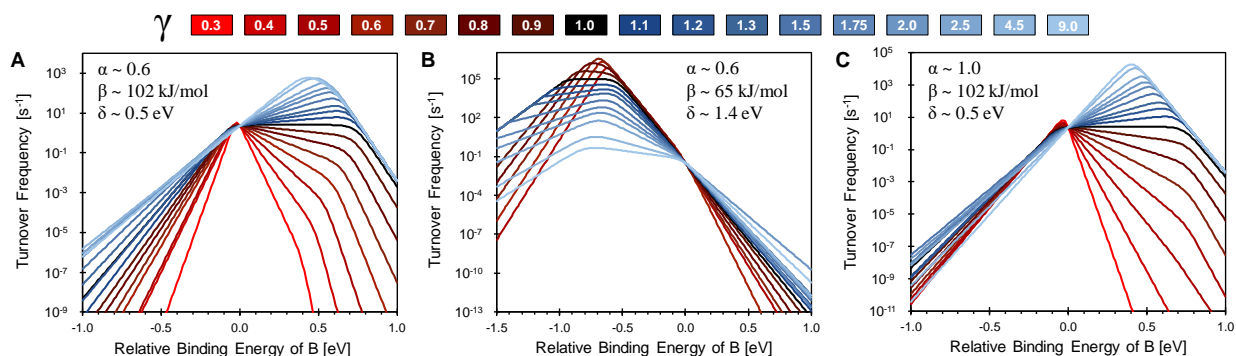
Figure 7. Parameter Variations Catalytic Reactions Depicted as Balandin-Sabatier SuperVolcanoes. A catalytic flow reactor reversibly converts A to B at 150 °C, 100 bar of pure feed A, and 1% yield of B. In each case, the heat of reaction was exothermic, $\Delta H_{rxn} \sim -20$ kJ/mol with varying gamma, $0.3 \leq \gamma_{B-A} \leq 9.0$. Surface parameters varying between cases included: **(A)** Alpha of 0.6, beta of 102 kJ mol^{-1}, and delta of 0.5 eV. **(B)** Alpha of 0.6, beta of 65 kJ mol^{-1}, and delta of 1.4 eV. **(C)** Alpha of 1.0, beta of 102 kJ mol^{-1}, and delta of 0.5 eV.

reaction rates. High γ_{B-A} curves coalesce on an adsorption line from 0.4 eV and lower values of relative binding energy of B.

Finally, α was raised from the intermediate value of 0.6 to its maximum value of 1.0, such that Figure 7C can be readily compared with Figure 7A since they share all other parameters in common. The maximum TOF_B was relatively unchanged, but all volcano curves in Figure 7C exhibit steeper slopes due to the influence of α. The tighter coalescence of all curves below 0.5 eV shows that these systems are largely adsorption limited due to a low δ of 0.5 eV. The desorption lines from 1.3 eV onwards for low γ systems are shifted to higher binding energies as compared with Figure 7A. This is due to the high coverage of A* at binding energies > 1.3 eV, and this limits the desorption TOF. In summary, the superVolcano shape and kinetic behavior is highly sensitive to both the transition state BEP relationship parameters and the binding energy equivalence point, δ. Since these parameters are a strong function of the reaction chemistry and metal crystal face/structure, practical application of dynamic catalysis will be guided by a combination of catalyst design and external stimulus selection to achieve beneficial catalytic reaction control.

3.4 Low Gamma Catalytic Kinetics. The dynamic kinetics of high gamma ($\gamma_{B-A} \sim 2.0$) catalytic systems were previously evaluated and shown to exhibit significant rate enhancement (1,000-10,000x above the Sabatier maximum) in the resonant frequency range[24]. Under optimal conditions, the surface coverage of high γ

chemistries oscillate between high coverage in A* and high coverage in B*, ultimately yielding a turnover frequency about equal to the imposed surface oscillation frequency. As these dynamic catalytic systems modulated into the strong binding state, the heat of the surface reaction was at its most negative condition leading to the lowest energy transition state; this permitted A* to readily convert to B*. When the surface binding energy then converted to weaker overall binding, the binding energy of B* decreased thereby decreasing the desorption barrier. Additionally, the high energy binding state inhibited the reverse surface reaction (B* to A*) due to a high transition state energy. This behavior held for multiple waveform types (e.g. square, sinusoidal) over a range of linear transition state scaling relationships ($0 < \alpha \leq 1.0$), making these types of reactions amenable to dynamic rate enhancement.

Low gamma ($\gamma_{B-A} < 1.0$) catalytic systems exhibit similar behavior with the variation of surface intermediate binding, but conditions leading to surface resonance remain to be identified. As depicted in Figure 8A, dynamic catalysis can lead to performance above the Sabatier maximum rate for low gamma systems. In this example, catalytic conversion of A-to-B occurs in a continuous-flow catalytic reactor at fixed temperature and pressure, and the system switches from static operation to five different dynamic frequencies for comparison ($f \sim 0.001, 0.035, 1.0, 10,$ and 1000 Hz, $\Delta U_B \sim 0.93$ eV). Oscillation frequencies above the Sabatier maximum rate (~ 0.036 s^{-1}) lead to high average turnover frequency
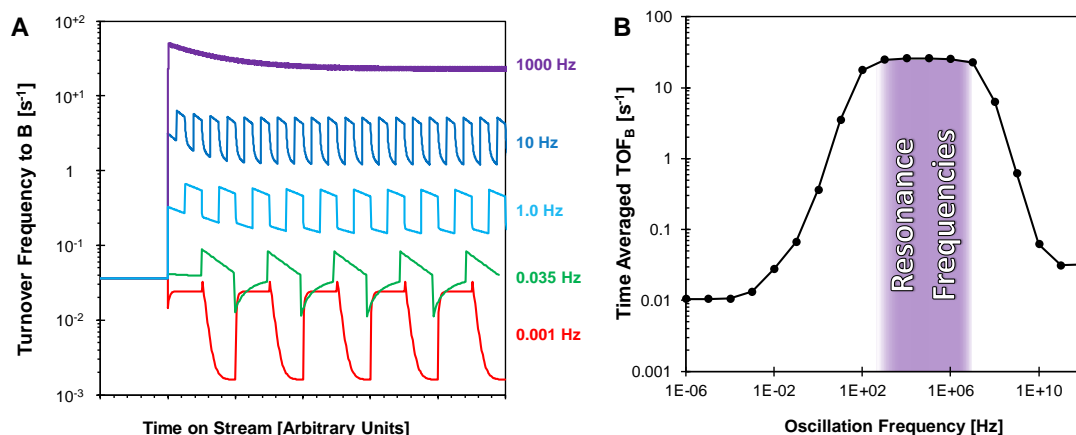
Figure 8. Kinetics of Low Gamma (γ ~ 0.5) Continuous Flow Catalytic Reactor. **(A)** A continuous flow reactor operating under static conditions exhibits $TOF_B \sim 0.036$ s^{-1}; implementation of catalyst dynamics at 0.001 Hz (red), 0.035 Hz (green), 1.0 Hz (light blue), 10 Hz (dark blue) and 1000 Hz (purple) varies the instantaneous TOF_B. **(B)** Continuous variation of the catalyst binding energy over varying frequencies ($10^{-6} < f < 10^{11}$ s^{-1}) reveals a band of resonance frequencies highlighted in purple. **Conditions:** T ~ 100 °C, P ~ 100 bar feed of A, $Y_B \sim 1\%$, $\Delta H_{rxn} \sim 0$ kJ mol^{-1}, α ~ 0.6, β ~ 102 kJ mol^{-1}, $\gamma_{B-A} \sim 0.5$, δ ~ 1.4 eV, $\Delta U_B \sim 0.93$ eV, [0.10 eV < U_B < 1.03 eV]

up to 25 s^{-1}. The depicted instantaneous TOF_B for each frequency shows flipping between high TOF_B and low TOF_B states due to the large change in surface coverages of A* and B*.

The low gamma system ($\gamma_{B-A} \sim 0.5$) of Figure 8B exhibits a broad range of resonance frequencies. For an oscillation amplitude of 0.93 eV, the TOF_B frequency response is shown in Figure 8B for a range of imposed square wave oscillation frequencies ($10^{-6} < f < 10^{12}$) in the binding energy of B*. From this plot, four corner frequencies can be determined as the transitions in slope; the resonant frequency range extends from about 10^2 to 10^7 Hz. Frequencies below 10^{-4} Hz yield a TOF of ~0.02 s^{-1}, which is the average of the steady state TOF at two oscillation endpoints, while frequencies above 10^{11} Hz yield the TOF from the starting condition (i.e. the volcano plot peak).

Figures 8A and 8B can be directly compared to the performance of the high gamma system ($\gamma_{B-A} \sim 2.0$) depicted in our previous publication[24]. At 0.001 Hz, the TOF_B response in Figure 8A exhibits an overshoot consistent with the flipping of the surface binding energies and off-loading of the surface. At intermediate frequencies (0.035, 1.0, and 10 Hz) in Figure 8A, the TOF_B response has sharp features due to rapid uptake of gas-phase species. In the resonant region (1000 Hz), a significant number of oscillations are required for the system to achieve steady state consistent with a gradual change in the surface coverages; for this

condition, there exists an initial overshoot of the average TOF_B above the final steady state value. This example indicates that the catalytic response of both low and high gamma systems, in this case $\gamma_{B-A} \sim 0.5$ and $\gamma_{B-A} \sim 2.0$, can exhibit similar general reaction behavior, with the caveat that any particular dynamic catalytic system must be evaluated to identify the conditions that permit resonance and rate enhancement. This key observation is relevant to general applicability of dynamics, since forward and reverse directions of any reaction will exhibit inverse values of gamma; this indicates that at least some catalytic systems could be dynamically promoted in either direction (forward or reverse) depending on the selected parameters of the imposed surface oscillation.

While both the forward and reverse directions of a reaction can be promoted dynamically, the strategies for selecting the parameters of the imposed surface binding energy oscillation between systems are indeed different. For the low gamma system ($\gamma_{B-A} \sim 0.5$) depicted in Figure 9A, the Sabatier curve is depicted in black with extended dashed lines above the Sabatier peak. The oscillation amplitude is depicted as a red bar with two endpoints: (i) the strong binding energy maximum is located at the position of the volcano peak, and (ii) the weak binding energy minimum is permitted to vary. The average turnover frequency to B is depicted in the heatmap of Figure 9B with variable square wave surface frequency and tunable

A

B

Turnover Frequency to B, TOF$_B$ [s^{-1}]

C

Turnover Frequency to B, TOF$_B$ [s^{-1}]
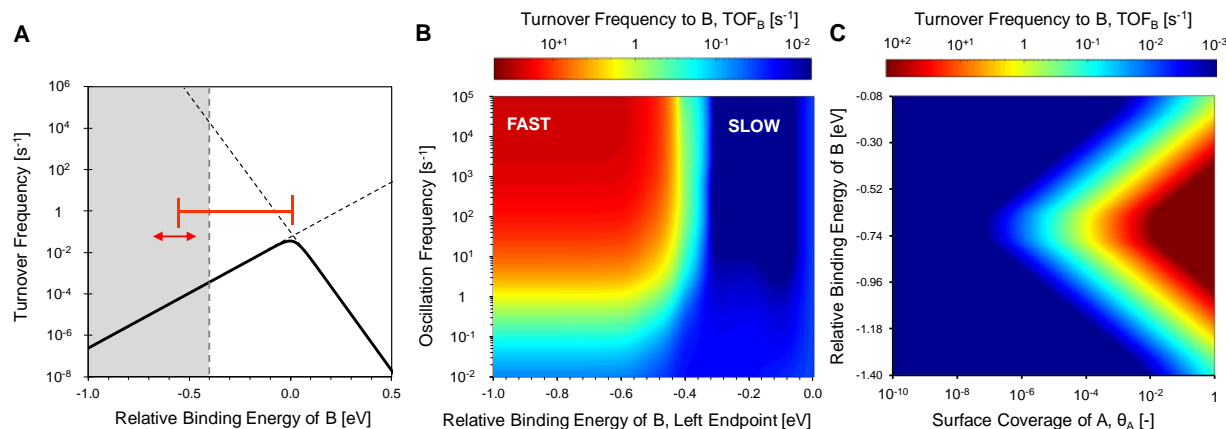
Figure 9. Catalytic Dynamics in a Flowing Stirred Tank Reactor at Differential Conversion with Variable Amplitude at Low Gamma. **(A)** Volcano kinetics of reversible A to B with variable amplitude. **(B)** Average turnover frequency to B (color distribution) as a function of square wave oscillation frequency and the amplitude low energy endpoint; the high energy endpoint is fixed at +1.03 eV. **(C)** Maximum possible surface reaction rate (color distribution) for A* reversibly converting to B* as a function of variable surface coverage and binding energies; negligible reverse reaction occurred under these conditions. **Conditions:** T~ 100 °C, P~100 bar A feed, Y_B ~ 1%, ΔH_{rxn} ~ 0 kJ mol^{-1}, α ~ 0.6, β ~ 102 kJ mol^{-1}, γ_{B-A} ~ 0.5, δ ~ 1.4 eV, and ΔU_B ~ variable.

minimum binding energy of B. Until the oscillation amplitude low binding energy endpoint (left) is less than -0.4 eV relative binding energy of B, the time averaged turnover frequency is negligible, and the A → B reaction is inhibited by dynamic catalysis. Above the -0.4-eV transition, the average turnover frequency to B is about constant and oscillation frequencies above 10^3 Hz lead to a high rate performance of 25 s^{-1} for a total rate enhancement of ~715x.

The importance of the transition at about -0.4 eV relative binding energy of B is indicative of the mechanism leading to dynamic enhancement. As shown in the surface coverage plot of Figure 6C, this transition is associated with the shift from a clean surface (θ_* ~ 1) to a surface covered in B* (θ_B ~ 1). When the oscillation amplitude extends into the low binding energy range associated with a clean surface, then B* is removed from the surface producing a dramatic reaction rate enhancement.

The significance of transitioning between a surface covered in reaction surface species and a clean surface for low gamma systems under dynamic conditions has implications for selection of catalyst materials. In general, the binding energies of A* and B* need to be sufficiently weak that all chemical species can be desorbed during the weaker of the surface oscillation states; in this case δ ~ 1.4 eV exhibited this capability. However, as the binding energy of B* varied with the imposed surface oscillation, a new limitation exists; the heat

of adsorption of both B* and A* must be less than or equal to zero. For low gamma systems, small variations in the binding energy of B* produce large variations in the binding energy of A* such that it readily approaches zero enthalpy of adsorption. This scenario can be interpreted by the gamma-delta plot of Figure 2B; as binding energies weaken; one surface species will achieve negligible adsorption enthalpy before the other one. In this scenario, the surface species with negligible adsorption enthalpy will remain in that state as the other surface species continues to change with the imposed oscillation.

The physical restriction of non-repulsive surfaces for adsorption alters the enthalpy of the surface reaction and the surface transition state energy by association. The implication is apparent in the TOF$_B$ heat map of Figure 9C, where the TOF$_B$ for the surface reaction elementary step is presented (color) as a function of the surface coverage of A (θ_A) and the relative binding energy of B [eV]. At low relative binding energies of B, the system exhibits a gradual change in the TOF$_B$ before a sharp transition above -0.7 eV; this transition is the condition where the binding energy of A approaches zero. Figure 9C also reveals part of the origin for fast dynamic TOF$_B$; at high surface coverage of A, the surface reaction can achieve TOF$_B$ of ~10^2 s^{-1}. These unique behaviors indicate that three-order-of-magnitude enhancement in rate is achievable for low gamma systems, but selection
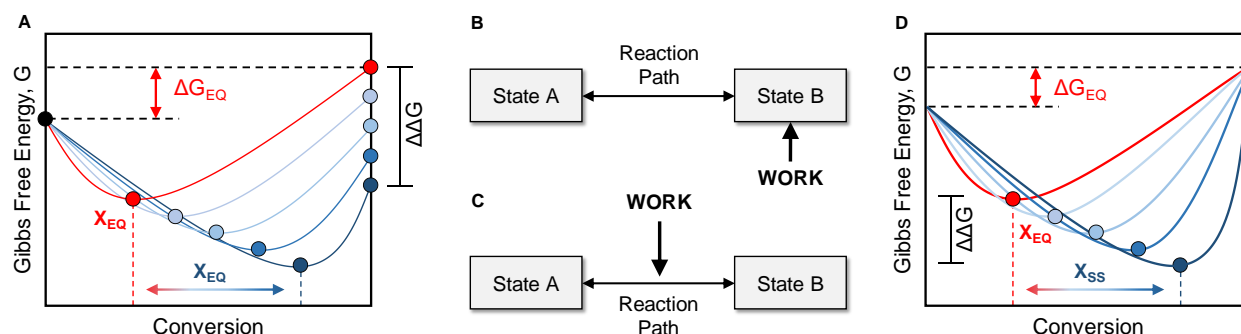
Figure 10. (A) Gibbs free energy landscape for a reaction with differing overall heats and entropy of reaction in state B, $\Delta\Delta G$. **(B)** Work applied to reactant state, B, alters the overall Gibbs free energy of reaction and the extent of conversion at equilibrium. **(C)** Work applied in the reaction path between reactant A and product B alters the Gibbs free energy minimum and extent of conversion at steady state. **(D)** General reaction system Gibbs free energy with respect to extent of conversion with added work, $\Delta\Delta G$, and minima identified as equilibrium points.

of the dynamic oscillation of surface binding energies must be carefully selected unique to each system.

3.5 Dynamic Steady State. As stated in the introduction, a grand challenge in catalysis and reaction engineering targets high yields of a desired product in the constraint of thermodynamic equilibrium and the mass action of Le Chatelier's principle. As shown in Figure 10A, reaction systems can be thought of as a thermodynamic trajectory between the reactant and product. Under thermodynamic control, the reaction system performance will approach the product composition where the overall free energy, or chemical potential, is minimized. Since each molecule has significantly different free energy due to varying chemical potentials, bonding, and functional groups, this free energy landscape is a strong function of the reaction chemistry.

The importance of controlling extent of reaction has led to the strategy depicted in Figure 10B; application of external work to one or both of the two thermodynamic states perturbs the free energy landscape in favor of a new equilibrium extent of conversion. For example, work via compression of reactant gases in chemistries such as hydrogenation of hydrocarbons alter the free energy landscape in favor of saturated bonds, requiring high pressure hydrogen as a co-reactant. Dynamic oscillation of surface binding energies potentially permits work to be imparted directly to the surface reaction (Figure 10C). Since work is applied directly to the surface reaction, the free energy landscape between A and B is modified without changing the free energy of the gas phase

species. A system of this type is depicted in Figure 10D, with the minimum energy offset from equilibrium by $\Delta\Delta G$. Thermodynamic work as a 'catalytic molecular pump' moving surface adsorbates from strong to weak binding could therefore permit reactor systems that achieve high catalytic conversion at thermodynamically unfavorable gas-phase conditions.

To assess catalytic reactor performance and extent of reaction of dynamic catalytic systems, simulations were conducted using a batch reactor charged with 100 bar of initial gas at varying composition of A and B with a fixed amount of catalyst with dynamically varying surface binding energies. Figure 11 depicts the time-resolved gas-phase composition within the catalytic batch reactor (100 bar, 250 °C) with seven different initial compositions of A and B. Dynamic surface binding energy of the catalyst was applied for 200 seconds of square wave of amplitude 0.5 eV and 1000 Hz, after which the system was converted to static catalysis (in this case at the volcano plot peak binding energy). Regardless of the initial gas-phase composition of the reactor, the system approached a dynamic steady state of 70 mol% B in the gas phase. While the small oscillatory behavior is difficult to observe in Figure 11, oscillation in the instantaneous TOF_B was observed upon zooming in on any of the data sets. Once the catalyst was converted from dynamic to static operation at 200 s, the system returned to thermodynamic equilibrium at 40 mol % B (ΔH_{ovr} of +2 kJ/gmol), indicating that deviation from equilibrium resulted from dynamic 'catalytic pumping' on the catalyst surface.
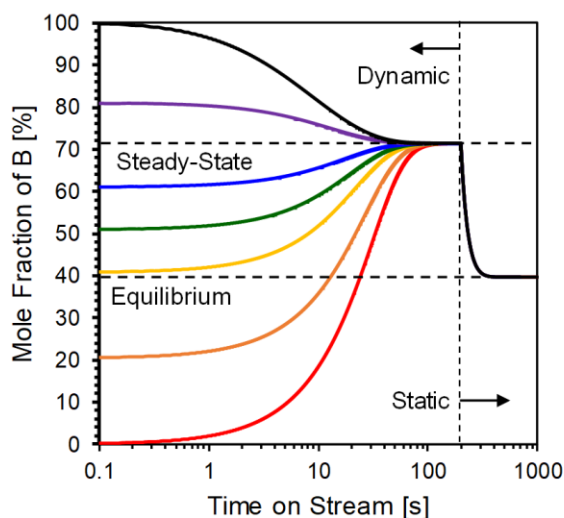
Figure 11. Dynamic Catalytic Reaction to Steady State Different from Equilibrium - High γ_{B-A} Condition. The reversible reaction of A to B undergoes dynamic catalytic conversion in a batch reactor at 250 °C, 100 bar total pressure, and a square waveform at 1000 Hz and 0.5 eV amplitude. Variable initial concentrations of component A. Surface chemistry parameters, $\alpha \sim 0.6$, $\beta \sim 135$ kJ mol^{-1}, $\gamma_{B-A} \sim 2.0$, $\delta \sim 1.0$ eV, and $\Delta H_{rxn} \sim +2.0$ kJ mol^{-1}.

3.6 Oscillatory Steady State of High γ Catalytic Systems. The steady state performance of a representative high gamma catalytic system ($\gamma_{B-A} \sim 2.0$, $\delta \sim 1.4$ eV) was assessed using a batch reactor model. Sabatier volcano plots for this system ($\alpha \sim 0.6$, $\beta \sim 102$ kJ/mol) are shown in Figure 12A, with reactor temperatures varying between 150-250 °C. Qualitatively, temperature does not change the shape and the rate-limiting kinetic regimes of the volcano plots. Similarly, the associated surface coverages for the considered system was plotted in Figure 12B for both A* and B*. B* dominated the surface at high relative binding energies while A* dominated at weaker binding energies. Each set of curves crossed over at the delta point, which is the equivalence point where A* and B* have the same energy. As temperature increased, the onset of surface vacancy shifted to stronger binding energies, and the remaining coverage of A* decreased faster with higher temperature (not shown, BE < -1.0 eV).

The extent of conversion at oscillatory steady state of the considered system of Figure 12 was evaluated as a function of applied square wave frequency *f*, waveform amplitude, and waveform

amplitude position. As depicted in Figure 12C at 150 °C, dynamic oscillation of the surface binding energy of B at a fixed amplitude can occur over a range of oscillation endpoints. The position of the strong binding energy of B endpoint was the independent variable in the heat maps of Figures 12D ($\Delta U_A \sim 0.5$ eV), 12E ($\Delta U_A \sim 1.0$ eV), and 12F ($\Delta U_A \sim 1.5$ eV), where the oscillatory steady state TOF$_B$ was determined via simulation.

In the simulations of Figure 12D-12F, the heat and entropy of reaction were zero, indicating that the system should achieve only 50% composition of both A and B in the gas phase (green) at thermodynamic equilibrium. However, the broad color range associated with the concentration at oscillatory steady state indicates that there exist catalytic conditions yielding substantial shift away from equilibrium as high as >99% yield of B for all oscillation frequencies above 1.0 Hz and oscillation endpoints above about 0.2 eV. This region of high conversion to B at steady state extends over a broad range that ends at lower oscillation endpoints before transitioning into a region favorable to forming the reactant species. Frequencies this slow and even as high as 0.1 Hz are achievable for all conceivable experimental methods of imposing oscillatory surface binding energy of adsorbates including oscillating electric fields and surface stress/strain.

The higher amplitude heat map plots of TOF$_B$ at $\Delta U_A \sim 1.0$ eV (Figure 12E) and $\Delta U_A \sim 1.5$ eV (Figure 12F) show enhanced performance at lower frequency (about 10^{-2} s^{-1}), because the amplitude oscillation endpoints move further and further away from the volcano plot peak. Moreover, there exists a sharp transition between the forward and backwards reaction at 0.4 eV relative binding energy, which exactly matches the absolute value of delta, $\delta \sim 1.4$ eV. High conversion to either A or B (>99%) is achievable at these higher amplitudes requiring only the selective application of surface binding oscillation at the relevant frequency and oscillation amplitude endpoints.

3.7 Oscillatory Steady State of Low γ_{B-A} Systems. Low gamma catalytic systems introduced in section 3.4 exhibited dramatic rate enhancement under dynamic operation (Figure 8) but with more complex kinetic behaviors as compared with high gamma systems in CSTR simulations. To assess the potential for controlling the extent of reaction of low gamma catalysis, a simulation with parameters
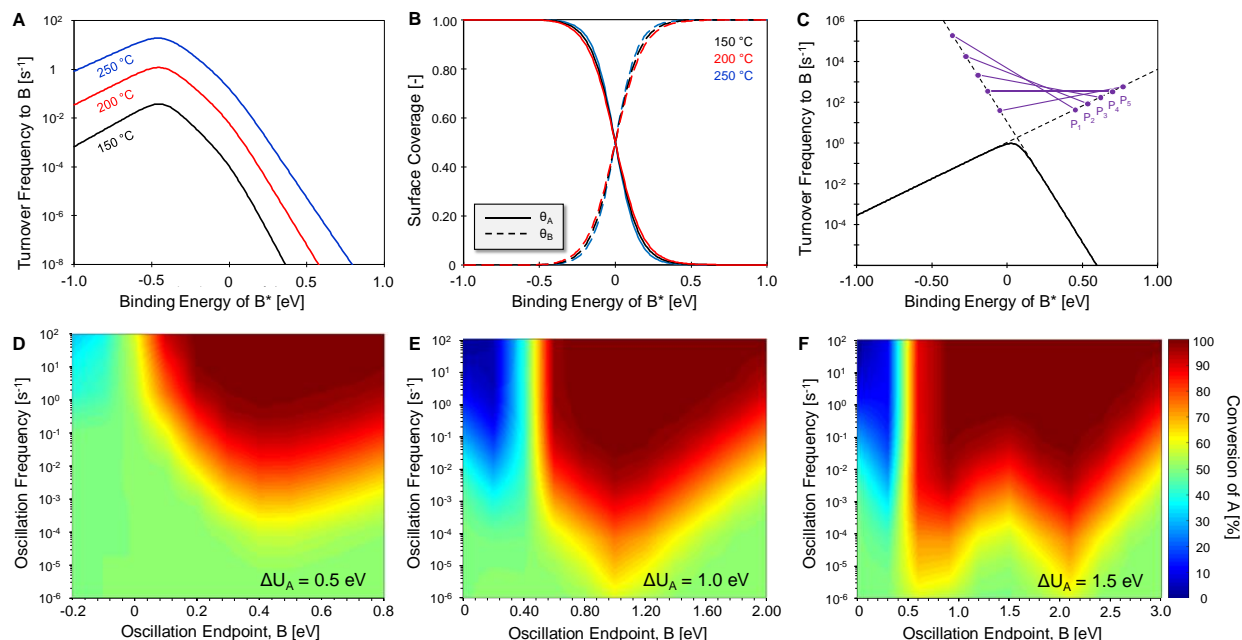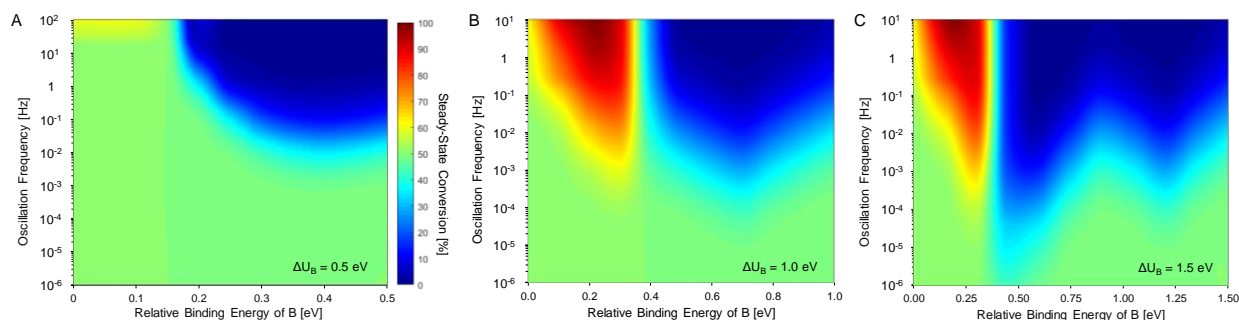
Figure 12. Dynamic Catalytic Conversion of A to B for High Gamma (γ ~ 2.0, δ ~ 1.4 eV). (A) Turnover frequency to product chemical B from reactant A for α ~ 0.6, β ~ 102 kJ/mol, and Y_B~1% for 150, 200, and 250 °C. **(B)** Surface coverages of A* (θ_A) and B* (θ_B) for α ~ 0.6 and Y_B~1% for 150, 200, and 250 °C. **(C)** Varying oscillation endpoints for ΔU_B ~ 0.8 eV. **(D/E/F)** Oscillatory steady state conversion of A (0 < X_A < 100%) at 150 °C and 100 bar for varying applied surface oscillation frequency and oscillation endpoint with oscillation amplitudes ΔU_A of 0.5, 1.0, and 1.5 eV

identical to the volcano plot of Figure 12A (except for a γ_{B-A} of 0.5) was conducted in a batch reactor with a square wave in surface binding energy oscillation. As depicted in Figure 13A-13C, three oscillation amplitudes of ΔU_B of 0.5, 1.0, and 1.5 eV were evaluated as a function of oscillation endpoints and frequency. Again, the simulated system reaction equilibrium was 50% composition (green in Figure 13) of both A and B.

For an oscillation amplitude of ΔU_B ~ 0.5 eV in Figure 13A, there exists a small region (yellow) where the forward A → B reaction is promoted between relative binding energies of B of 0-0.2 eV and about 10^2 Hz. However, above about 0.15 eV of relative binding energy of B exists a large region (dark blue) overwhelmingly favorable to the reverse reaction (formation of A). Higher oscillation amplitudes in low gamma γ_{B-A} catalytic systems again lead to high conversion at oscillatory steady state, in this case for both reaction directions as yields > 90 % B are observed while other oscillation endpoints yield > 99 % A. The two regions are split by the delta point (δ ~ 1.4 eV, 0.4 relative binding energy of B). The implication is that this system can be tuned to produce an outlet

stream with nearly completely controllable composition at high reactor residence times, just by varying the oscillation endpoints at frequencies between 1-10 Hz. The high and low conversion regimes exist as low as 0.001 Hz making them accessible to slowly oscillating systems. This behavior is nearly identical to the high gamma system in Figure 12; as the only difference between Figure 12 and 13 being the inverse values of gamma (γ_{B-A} of 2.0 and 0.5, respectively), this inverse mirrored behavior is expected. Both low and high gamma systems provide versatility in conversion as nearly pure product streams of A or B can be produced by merely changing the dynamic catalysis oscillation endpoints relative to the catalytic chemistry delta point.

3.8 Mechanism of Catalytic Molecular Pumping. The tunable directionality (forward versus reverse) of catalytic molecular pumping observed in Figures 12 and 13 derives from the mechanism of molecular movement through the oscillating energy profiles on the catalytic surface. As shown earlier, catalytic systems can be driven in the forward or reverse directions by selection of the catalytic material or stimulus method (affecting α,

Figure 13. Dynamic Catalytic Conversion of A to B for Low Gamma ($\gamma_{B-A} \sim 0.5$, $\delta \sim 1.4$ eV). Steady-state average conversion of A-to-B in a batch reactor (equilibrium at 50% - green) for varying square wave amplitude high binding energy state [eV] and oscillation frequency [Hz] for fixed amplitudes ΔU_B of: **(A)** 0.5 eV, **(B)** 1.0 eV, and **(C)** 1.5 eV. Batch reactor conditions: 150 °C, initial reactor composition of 100 bar pure A, $\Delta H_{rxn} \sim 0$ kJ mol^{-1}, $\alpha \sim$ 0.6, $\beta \sim 102$ kJ mol^{-1}, $\gamma_{B-A} \sim 0.5$, and $\delta \sim 1.4$ eV.

β, γ, and δ) but also by the selection of imposed surface oscillation including the frequency, amplitude, and amplitude endpoints. The relationship between selected parameters and catalytic pumping directionality is depicted in Figure 14 for the system previously described in Figure 13 with a low gamma ($\Delta H_{ovr} \sim 0$ kJ gmol^{-1}, $\alpha \sim 0.6$, $\beta \sim 102$ kJ gmol^{-1}, $\gamma_{B-A} \sim 0.5$, and $\delta \sim 1.4$ eV). Two conditions were selected; Figure 14A-B correspond to an oscillation amplitude promoting the reverse reaction, while Figure 14C-D has an amplitude promoting the forward reaction. In each energy diagram (Figure 14A, 14C), the amplitude minimum (U_{min}, blue) and maximum (U_{max}, red) are depicted along with the relative binding energy of B* corresponding to the Sabatier peak under static conditions (purple, dashed) and the binding energy associated with delta (black, $\delta \sim 1.4$ eV).

The directionality of the dynamic catalytic system is visually apparent from the values of the enthalpy of A* and B* at the minimum amplitude (U_{min}). The reverse reaction (B-to-A) is favored when A* is lower in energy than B* at U_{min} in Figure 14A, while the forward reaction (A-to-B) is favored when B* is lower in energy than A* at U_{min} in Figure 14C. By this interpretation, the lower energy state U_{min} serves as the condition whereby the surface reaction proceeds to accumulate A* or B* on the surface; the higher energy state U_{max} then serves to push this surface reaction product into the gas phase. In the low energy state U_{min}, the transition state enthalpy must be lower than the desorption enthalpy to permit the surface reaction to proceed. This general behavior is depicted in the

schemes for the reverse reaction (Figure 14B) and forward reaction (Figure 14D).

Interpreting general reaction systems for potential catalytic molecular pumping relies on the determination of the reaction energy profile under different oscillation conditions with respect to the parameter delta, δ. These intermediate and transition state energies can now be determined computationally for almost any catalytic system[66]. As defined earlier, the quantity delta δ identifies the adsorption enthalpy whereby both A* and B* have equal binding energy with the surface. Delta therefore serves as a separation point between the forward and reverse directionality of catalytic molecular pumping; for any system with a non-unity gamma, the surface species of lowest energy (A* or B*) will differ for systems operating on either side of delta. This precise transition in directionality was observed in Figures 12 and 13, where the shift from high to low conversion was demarcated by the relative binding energy of B* equaling delta.

3.9 Efficiency of Dynamic Catalysis at Oscillatory Steady State. Returning to the concept of imparting work during catalysis as described in Figure 10C, the observed free energy change for the reaction ($\Delta\Delta G$) is related to the applied oscillation amplitude (ΔU_i). In mechanical applications, this relationship is typically expressed as an efficiency, which compares the applied work (i.e. energy units after integrating over time) to the resulting change in system enthalpy, internal energy, or another indicator such as temperature. Here, the efficiency of the dynamic catalytic system is defined as,
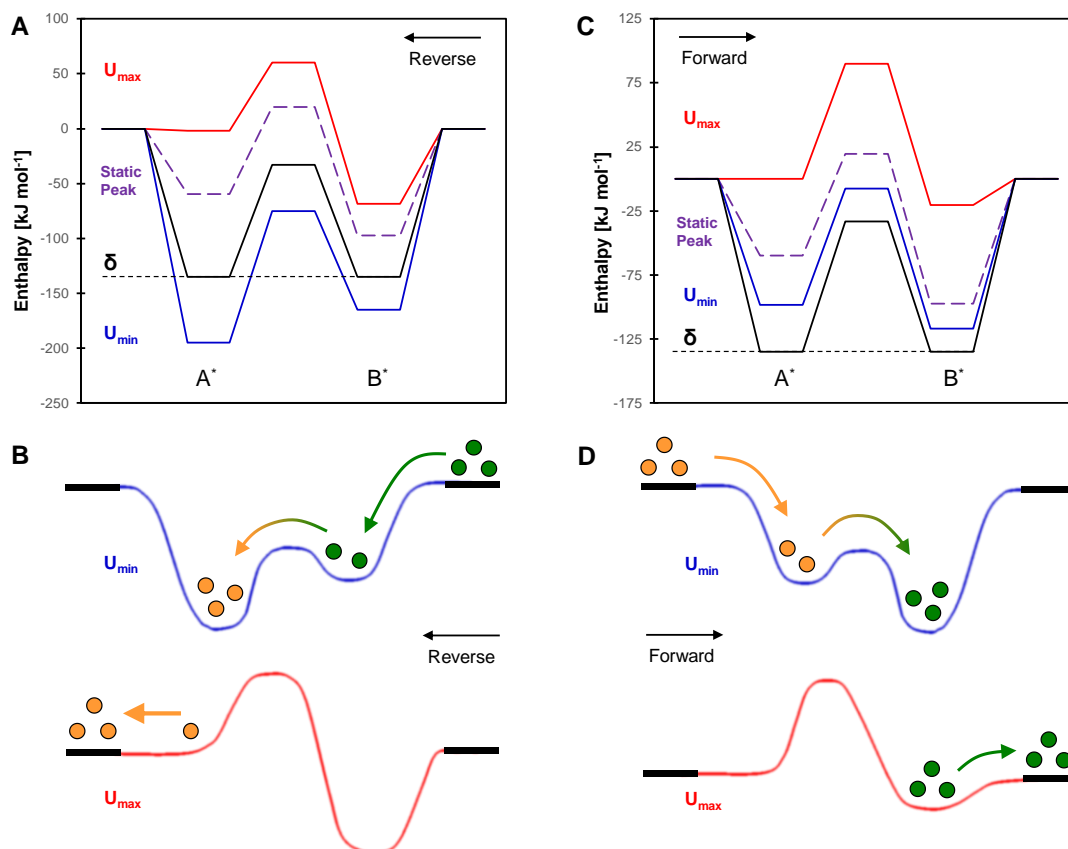
Figure 14. Mechanism of Catalytic Molecular Pumping and Rate Enhancement. Energy diagrams for catalytic unimolecular reaction system with reaction chemistry defined as: $\Delta H_{ovr} \sim 0$ kJ gmol^{-1}, $\alpha \sim 0.6$, $\beta \sim 102$ kJ gmol^{-1}, $\gamma_{B-A} \sim 0.5$, and $\delta \sim 1.4$ eV. **(A)** Oscillation amplitude of 1.0 eV with oscillation endpoints of B* of $U_{min} \sim 0.6$ eV and $U_{max} \sim 1.6$ eV. **(B)** For the selected oscillation amplitude, the catalytic molecular pump moves molecules of B in green through adsorption to B* and then reaction to A*; subsequent oscillation desorbs A* to A. **(C)** Oscillation amplitude of 1.0 eV with oscillation endpoints of B* of $U_{min} \sim 0.2$ eV and $U_{max} \sim 1.2$ eV. **(D)** For the selected oscillation amplitude, the catalytic molecular pump moves molecules of A in orange through adsorption to A* and then reaction to B*; subsequent oscillation moves molecules of B* to product B in the gas phase.

$$\varepsilon = \frac{|\Delta\Delta G|}{\Delta U_i} = \frac{Free\ Energy\ Deviation}{Applied\ Oscillation\ Amplitude}$$
(10)

The efficiency is the absolute value of the free energy deviation from equilibrium to account for both the forward and reverse reaction promotion at oscillatory steady state relative to the applied oscillation amplitude. For consistency with the mechanism of dynamic catalysis of Figure 14, the amplitude in the denominator of the efficiency (ΔU_A or ΔU_B) was selected based on the directionality of the promoted reaction; ΔU_B was selected for the forward reaction, and ΔU_A was selected for the reverse reaction.

Representative high and low gamma systems were analyzed to assess the efficiency as a function of oscillation amplitude, waveform, and endpoint selection. As demonstrated in a previous publication for a continuous flow reactor under dynamic catalysis operation[24], oscillation waveform shape has a significant effect on dynamic catalysis rate promotion. In the CSTR for a high gamma system ($\gamma_{B-A} \sim 2.0$), the square waveform exhibited the highest TOF$_B$ followed by sinusoidal (2-3x slower) and then triangle and sawtooth waveforms (4-6x slower). As shown in Figure 15, these waveform types were applied to the batch reactor system, and the resulting steady state composition was compared with the thermodynamic equilibrium composition (50% A and B in all cases). The $\Delta\Delta G$ was computed as the difference in the apparent free energy of the
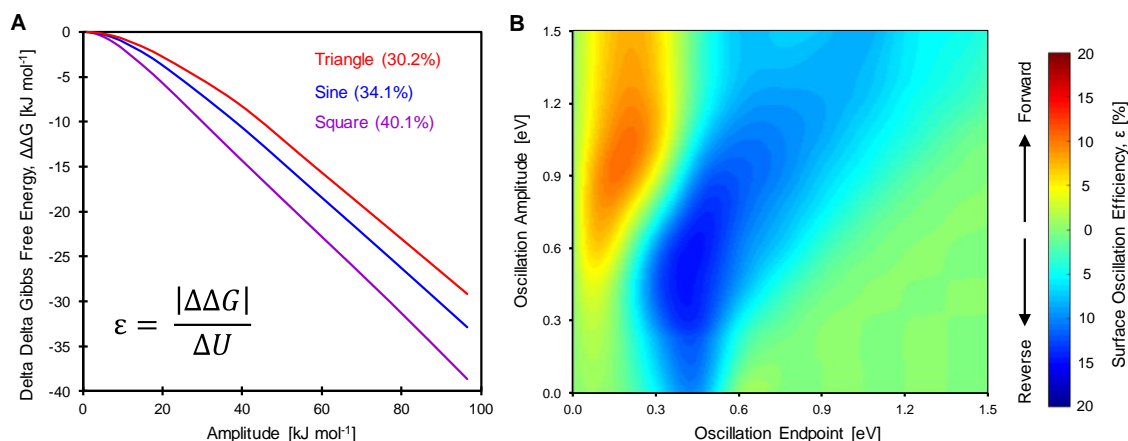
Figure 15. Conversion Efficiency of A-to-B Reaction on Dynamic Catalytic Surfaces. (A) Square, sinusoidal, or triangle wave with varying amplitude operating at 10 Hz ($\alpha \sim 0.6$, $\beta \sim 135$ kJ mol^{-1}, $\gamma \sim 2.0$, $\delta \sim 1.0$ kJ mol^{-1}, and $\Delta H_{ovr} \sim 0$ kJ mol^{-1}) on a catalyst in a batch reactor at oscillatory steady state offset from equilibrium by delta delta Gibbs free energy, $\Delta\Delta G$. The efficiency is defined as the absolute value of $\Delta\Delta G$ relative to the oscillation amplitude, ΔU. **(B)** The surface oscillation efficiency (ε, color map) of a square wave operating at 1.0 Hz with varying amplitude and oscillation amplitude endpoint exhibits two bands of increased efficiency ($\alpha \sim 0.6$, $\beta \sim 102$ kJ mol^{-1}, $\gamma \sim 0.5$, $\delta \sim 1.4$ kJ mol^{-1}, and $\Delta H_{ovr} \sim 0$ kJ mol^{-1}).

reaction at oscillatory steady state from the actual equilibrium (i.e., 50% A and 50% B).

Figure 15A shows the efficiency of the applied waveforms as a function of imposed amplitude at a constant frequency of 10 Hz. Initially, near zero amplitude, the efficiency is low for all waveforms as shown by the shallow slope of the plot. Once the oscillation amplitude achieves 10-20 kJ mol^{-1} (i.e. 0.1-0.2 eV), the relationship between $\Delta\Delta G$ and ΔU is effectively described by a straight line. The slope of this line is the system efficiency during dynamic catalysis since it is the ratio of two energy units. The maximum efficiency observed was ~40 % for the square wave with the sinusoidal and triangular wave being slightly less effective at 34% and 30%, respectively.

Due to the importance of oscillation amplitude endpoints in low gamma γ_{B-A} catalytic systems, the efficiency of low gamma systems was evaluated in Figure 15B as a function of both oscillation amplitude and oscillation amplitude endpoint in a flow reactor. As observed in the low gamma batch reactor results in Figure 13A-13C, the forward A $\rightarrow$ B reaction (yellow-to-red) was only enhanced at oscillation endpoints up to the delta point. Once stronger binding energies were imposed on the system, the B $\rightarrow$ A reaction (blue) was highly favorable due to the dominant surface coverage of A*. The highest observed efficiency here was ~16 %, specifically for the B $\rightarrow$ A reaction.

A parity region was observed in Figure 15B that runs diagonally along the blue color-coded B $\rightarrow$ A region with a slope of about unity. This region traces points where the difference between the oscillation endpoint and amplitude equals delta. Once this difference was less than delta (i.e. the lower right quadrant of the heat map), the system performance rapidly declined to 0% efficiency (green). This inefficiency resulted from the surface coverage which needs to be turned over significantly to enhance reactor performance, and the delta point determines the crossover between A* and B* covered surfaces. In summary, the system efficiency for high gamma and low gamma cases is a strong function of oscillation amplitude, frequency, and endpoint selection but waveform shape also has a minor effect.

3.10 Catalytic Molecular Pump and Molecular Machines. The design of molecules with dynamic functionality has been extensively described as 'molecular machines'[67] with both synthetic and biological examples[68,69]. While 'switchable catalysts' are capable of turning on and off as needed[70], other molecular machines and molecular devices are capable of implementing motion including molecular motors and pumps[68,71,72]. For example, an artificial molecular pump is capable of moving molecules such as charged rings up a concentration gradient[73], conceptually similar to nature's capability for

controlling the mobility of metal ions across membranes against equilibrium[74]. These molecular machines and pumps are relevant to the dynamic oscillating catalyst surface concept addressed in this work due to a common mechanism. Of the many methods of manipulating molecules, many molecular machines and pumps utilize energy to implement a dynamic 'pulsating' ratchet energy profile[75,76,77]. Similar to Figure 14, progression along a pulsating ratchet permits molecules to spontaneously access the current low energy states; the input of energy into the ratchet system alters the free energy landscape permitting molecules to access new low energy states that constitute progress in position (i.e., molecular pumps). The evolution of changing energy profiles biases progress in one direction based on local peak heights, consistent with its 'ratchet' name[73].

Molecular pumps and 'catalytic pumps' share a common purpose; move molecules against thermodynamics. Molecular pumps move molecules against the free energy gradient associated with concentration or pressure, while the catalytic pumps described here aim to advance the extent of reaction against the chemical potential associated with chemical reaction equilibrium. Molecular pumps utilize the ratchet mechanism, while the catalytic pump utilizes the ratchet mechanism plus the addition of a surface reaction as one of the free energy profile transition states. Similarly, molecular pumps utilize external energy sources (e.g. ATP in biological membrane transport), while catalytic pumps oscillate binding energy by a variety of proposed methods as described in Figure 4 (e.g., oscillating surface strain or electric field).

4.0 Conclusions. The dynamic catalytic promotion of A-to-B surface reactions permits order-of-magnitude rate enhancement and control of extent of conversion for a broad set of surface mechanisms. Classification of surface mechanisms and their associated kinetic behavior requires detailed description of the key parameters defined here as gamma (γ, the ratio of variation in surface adsorbate binding energy) and delta (δ, the surface adsorbate binding energy common to two intermediates). High gamma catalytic systems ($\gamma > 1$) achieve surface resonance between an oscillating external stimulus and an oscillating surface reaction by selecting a catalyst and dynamic conditions that maintain two oscillating states of A* and B*, respectively. Alternatively, low gamma catalytic systems ($\gamma < 1$) require one of the two oscillating states to consist of a completely bare surface (open sites only). The two different dynamic catalytic behaviors are visually apparent in their Sabatier volcano shapes; superposition of numerous Sabatier volcanoes with varying γ comprise a 'supervolcano' where the regime of surface-reaction rate control is visible as deviation from the superVolcano border. Dynamic catalysis was also show to serve as a 'catalytic molecular pump' by altering the binding energy of surface adsorbate species via external work. The extent of work converted into catalytic conversion deviating from equilibrium was defined as the dynamic catalytic efficiency. For both low and high γ catalytic systems, conditions of efficient catalytic promotion as high as 30-40% were identified as a strong function of the selected dynamic oscillation conditions of frequency, amplitude, and waveform type.

Supporting Information. Additional information including computer code, time-on-stream data, and simulation methods are included in the supporting information.

References

[1] U.S. Department of Energy. "Basic Research Needs for Catalysis Science to Transform Energy Technologies: Report from the U.S. Department of Energy, Office of Basic Energy Sciences Workshop May 8-10, 2017, in Gaithersburg, Maryland". Retreived Feb. 3, 2017. Link: https://science.energy.gov/~/media/bes/pdf/reports/2017/BRN_CatalysisScience_rpt.pdf

[2] C.L. Williams, C.C. Chang, P. Do, N. Nikbin, S. Caratzoulas, D.G. Vlachos, R.F. Lobo, W. Fan, P.J. Dauenhauer, "Cycloaddition of biomass-derived furans for catalytic production of renewable p-xylene," *ACS Catalysis* **2012**, 2(6), 935-939.

[3] O.A. Abdelrahman, D.S. Park, K.P. Vinter, C.S. Spanjers, L. Ren, H.J. Cho, K. Zhang, W. Fan, M. Tsapatsis, P.J. Dauenhauer, "Renewable isoprene by sequential hydrogenation of itaconic acid and dehydra-decyclization of 3-methyl-tetrahydrofuran," *ACS Catalysis* **2017**, 7(2), 1428-1431.

[4] D.J. Saxon, M. Nasiri, M. Mandal, S. Maduskar, P.J. Dauenhauer, C.J. Cramer, A.M. LaPointe, T.M. Reineke, "Architectural control of isosorbide-based polyethers via ring-opening polymerization," *Journal of the American Chemical Society* **2019**. DOI: 10.1021/jacs.9b00083

[5] J.A. Rodriguez, P. Liu, D.J. Stacchiola, S.D. Senanayake, M.G. White, J.G. Chen, "Hydrogenation of CO_2 to methanol: Importance of metal-oxide and metal-carbide interfaces in the activation of CO_2," *ACS Catalysis* **2015**, 5(11), 6696-6706.

[6] M. Dunwell, W. Luc, Y. Yan, F. Jiao, B. Xu, "Understanding surface-mediated electrochemical reactions: CO2 reduction and beyond," *ACS Catalysis* **2018**, 8(9), 8121-8129.

[7] M. Hattori, T. Mori, Y. Inoue, M. Sasase, T. Tada, M. Kitano, T. Yokoyama, M. Hara, H. Hosono, "Enhanced catalytic ammonia synthesis with transformed BaO," *ACS Catalysis* **2018**, 8(12), 10977-10984.

[8] B. Lin, L. Heng, B. Fang, H. Yin, J. Ni, X. Wang, J. Lin, L. Jiang, "Ammonia synthesis activity of alumina-supported ruthenium catalyst enhanced by alumina phase transformation," *ACS Catalysis* **2019**, 9(3), 1635-1644.

[9] A.R. Singh, J.H. Montoya, B.A. Rohr, C. Tsai, A. Vojvodic, J.K. Norskov, "Computational design of active site structures with improved transition-state scaling for ammonia synthesis," *ACS Catalysis* **2018**, 8(5), 4017-4024.

[10] J.W. Erisman, M.A. Sutton, J. Galloway, Z. Klimont, W. Winiwarter, "How a century of ammonia synthesis changed the world," *Nature Geoscience* **2008**, 1, 636-639.

[11] U. Deka, I. Lezcano-Gonzalez, B.M. Weckhuysen, A.M. Beale, "Local environment and nature of Cu active sites in zeolite-based catalysts for the selective catalytic reduction of NOx," *ACS Catalysis* **2013**, 3(3), 413-427.

[12] H. Yuan, J. Chen, H. Wang, P. Hu, "Activity trend for low-concentration NO oxidation at room temperature on rutile-type metal oxides," *ACS Catalysis* **2018**, 8(11), 10864-10870.

[13] J. Liu, D. Zhu, Y. Zheng, A. Vasileff, S. Qjao, "Self-supported earth-abundant nanoarrays as efficient and robust electrocatalysts for energy-related reactions," *ACS Catalysis* **2018**, 8(7), 6707-6732.

[14] J.E. Sutton, D.G. Vlachos, "A theoretical and computational analysis of linear free energy relations for the estimation of activation energies," *ACS Catalysis* **2012**, 2, 1624-1634.

[15] R.R. Chianelli, G. Berhault, P. Raybaud, S. Kasztelan, J. Hafner, H. Toulhoat, "Periodic trends in hydrodesulfurization: in support of the Sabatier principle," *Applied Catalysis A: General* **2002**, 227(1-2), 83-96.

[16] A. Logadottir, T.H. Rod, J.K. Norskov, B. Hammer, S. Dahl, C.J.H. Jacobsen, "The Bronsted-EvansPolyanyi relation and the volcano plot for ammonia synthesis over transition metal catalysts," *Journal of Catalysis* **2001**, 197, 229-231.

[17] S. Ichikawa, "Volcano-shaped curves in heterogeneous catalysis," *Chemical Engineering Science* **1990**, 45(2), 529-535.

[18] A.K. Vijh, "Sabatier-Balandin interpretation of the catalytic decomposition of nitrous oxide on metaloxide semiconductors," *Journal of Catalysis* **1973**, 31, 51-54.

[19] D.A. Hansgen, D.G. Vlachos, J.G. Chen, "Using first principles to predict bimetallic catalysts for the ammonia decomposition reaction," Nature Catalysis 2010, 2(6), 484-489.

[20] A.W. Ulissi, A.J. Medford, T. Bligaard, J.K. Norskov, "To address surface reaction network complexity using scaling relations maching learning and DFT calculations," *Nature Communications* **2017**, 8, 14621.

[21] J.E. Sutton, D.G. Vlachos, "Effect of errors in linear scaling relations and Bronsted-Evans-Polanyi relations on activity and selectivity maps," *Journal of Catalysis* **2016**, 338, 273-283.

[22] J.K. Norskov, T. Bligaard, J. Rossmeisl, C.H. Christensen, "Towards the computational design of solid catalysts," *Nature Chemistry* **2009**, 1, 37-46.

[23] F. Calle-Vallejo, D. Loffreda, M.T.M. Koper, P. Sautet, "Introducing structural sensitivity into

adsorption-energy scaling relations," *Nature Chemistry* **2015**, 7, 403-410.

[24] W.A. Ardagh, O. Abdelrahman, P.J. Dauenhauer, "Principles of Dynamic Heterogeneous Catalysis: Surface Resonance and Turnover Frequency Response," *ACS Catalysis* **2019**, 9, 6929-6937.

[25] A.A. Balandin, V.A. Ferapontov, A.A. Tolstopyatova, "The activity of cadmium oxide as a catalyst for hydrogen dehydrogenation," *Bulletin of the Academy of Sciences of the USSR, Division of Chemical Science.* **1960**, 9(10), 1630-1636.

[26] A.A. Balandin, "The multiplet theory of catalysis. Energy factors in catalysis," 1964, 33(5), 549-579.

[27] J.R. Jennings. Catalytic Ammonia Synthesis: Fundamentals and Practice. 1991, Springer Science, New York. DOI: 10.1007/978-1-4757-9592-9. ISBN 978-1-4757-9594-3

[28] J.L. Colby, P.J. Dauenhauer, B.C. Michael, A. Bhan, L.D. Schmidt, "Improved utilization of biomass-derived carbon by co-processing with hydrogen-rich feedstocks in millisecond reactors," *Green Chemistry* **2010**, 12, 378-380.

[29] L.C. Grabow, M. Mavrikakis, "Mechanism of methanol synthesis on Cu through CO_2 and CO hydrogenation," *ACS Catalysis* **2011**, 1(4), 365-384.

[30] D. Pakhare, J. Spivey, "A review of dry (CO2) reforming of methane over noble metal catalysts," *Chemical Society Reviews* **2014**, 43, 7813-7837.

[31] Q. Fu, H. Saltsburg, M. Flytzani-Stephanopoulos, "Active nonmetallic Au and Pt species on Ceria-based water-gas shift catalysts," *Science* **2003**, 301(5635), 935-938.

[32] G. Marnellos, M. Stoukides, "Ammonia synthesis at atmospheric pressure," *Science* **1998**, 282(5386), 98-100.

[33] G. Ertl, "Surface Science and Catalysis – Studies on the Mechanism of Ammonia Synthesis: The P.H. Emmett Award Address," *Catalysis Reviews Science and Engineering* **1980**, 21(2), 201-223.

[34] C. Ratnasamy, J.P. Wagner, "Water Gas Shift Catalysis," *Catalysis Reviews* **2009**, 51, 325-440.

[35] D.S. Newsome, "The Water-Gas Shift Reaction," *Catalysis Reviews Science and Engineering* **1980**, 21(2), 275-318.

[36] F. Cavani, N. Ballarini, A. Cericola, "Oxidative dehydrogenation of ethane and propane: How far from commercial implementation?" *Catalysis Today* **2007**, 127(1-4), 113-131.

[37] M. Malmali, Y. Wei, A. McCormick, E.L. Cussler, "Ammonia synthesis at reduced pressure via reactive separation," *Industrial & Engineering Chemistry Research* **2016**, 55(33), 8922-8932.

[38] C. Smith, A.V. McCormick, E.L. Cussler, "Optimizing the conditions for ammonia production using absorption," *ACS Sustainable Chemistry & Engineering* **2019**, 7(4), 4019-4029.

[39] C.L. Williams, C.C. Chang, P. Do, N. Nikbin, S. Caratzoulas, D.G. Vlachos, R.F. Lobo, W. Fan, P.J. Dauenhauer, "Cycloaddition of biomass-derived furans for catalytic production of renewable p-xylene," *ACS Catalysis* **2012**, 2(6), 935-939.

[40] C.L. Williams, K.P. Vinter, C.C. Chang, R. Xiong, S.K. Green, S.I. Sandler, D.G. Vlachos, W. Fan, P.J. Dauenhauer, "Kinetic Regimes in the tandem reactions of H-BEA catalyzed formation of p-xylene from dimethylfuran," *Catalysis Science and Technology* **2016**, 6, 178-187.

[41] L.C. Buelens, V.V. Galvita, H. Poelman, C. Detavernier, G.B. Marin, "Super-dry reforming of methane intensifies CO_2 utilization via Le Chatelier's principle," *Science* **2016**, 354(6311), 449-452.

[42] W. Lin, C.J. Murphy, "A demonstration of Le Chatelier's Principle on the nanoscale," *ACS Central Science* **2017**, 3(10), 1096-1102.

[43] I. Roger, M.A. Shipman, M.D. Symes, "Earth-abundant catalysts for electrochemical and photoelectrochemical water splitting," *Nature Reviews Chemistry* **2017**, 1, 0003.

[44] D. Todd, M. Schwager, W. Merida, "Thermodynamics of high-temperature, high-pressure water electrolysis," *Journal of Power Sources* **2014**, 269, 424-429.

[45] B.H.R. Suryanto, H.L. Du, D. Wang, J. Chen, A.N. Simonov, D.R. MacFarlane, "Challenges and prospects in the catalysis of electroreduction of nitrogen to ammonia," *Nature Catalysis* **2019**, 2, 290-296.

[46] A. Ardagh, O. Abdelrahman, P.J. Dauenhauer, "Principles of Dynamic Heterogeneous Catalysis: Surface Resonance and Turnover Frequency Response," *ChemRxiv*, March 1, **2019**. doi.org/10.26434/chemrxiv.7790009.v1

[47] J.E. Sutton, D.G. Vlachos, "A theoretical and computational analysis of linear free energy relations for the estimation of activation energies," *ACS Catalysis* **2012**, 2(8), 1624-1634.

[48] M. Mavrikakis, B. Hammer, J.K. Norskov, "Effect of strain on the reactivity of metal surfaces," *Physical Review Letters* **1998**, 81(13), 2819.

[49] Y. Xu, M. Mavrikakis, "Adsorption and dissociation of O2 on Cu(111): thermochemistry, reaction barrier and the effect of strain," *Surface Science* **2001**, 494, 131-144.

[50] Z. Xia, S. Guo, "Strain engineering of metal-based nanomaterials for energy electrocatalysis," *Chemical Society Reviews*, **2019**, 48, 3265-3278. DOI: 10.1039/c8cs00846a

[51] J. Weissmuller, "Adsorption-strain coupling at solid surfaces," *Current Opinion in Chemical Engineering* **2019**, 24, 45-53.

[52] A.J. Bennett, "The effect of applied electric fields on chemisorption," *Surface Science* **1975**, 50, 77-94.

53 M.T.M. Koper, R.A. van Santen, "Electric field effects on CO and NO adsorption at the Pt(111) surface," *Journal of Electroanalytical Chemistry* **1999**, 476, 64-70.

54 S.A. Wasileski, M.T.M. Koper, M.J. Weaver, "Field-Dependent Chemisorption of Carbon Monoxide on Platinum-Group (111) Surfaces: Relationships between Binding Energetics, Geometries, and Vibrational Properties as Assessed by Density Functional Theory" *J. Phys. Chem. B* **2001**, 105, 3518-3530.

55 Y. Wang, C.H. Kim, Y. Yoo, J.E. Johns, C.D. Frisbie, "Field effect modulation of heterogeneous charge transfer kinetics at back-gated twodimensional MoS2 electrodes," *Nano Letters* **2017**, 17, 7586-7592.

56 C.H. Kim, C.D. Frisbie, "Field effect modulation of outer-sphere electrochemistry at back-gated, ultrathin ZnO electrodes," *Journal of the American Chemical Society* **2016**, 138, 7220-7223.

57 C.H. Kim, Y. Wang, C.D. Frisbie, "Continuous and reversible tuning of electrochemical reaction kinetics on back-gated 2D semiconductor electrodes: steady state analysis using a hydrodynamic method," *Analytical Chemistry* **2019**, 91, 1627-1635.

58 P. Deshlahra, W.F. Schneider, G.H. Bernstein, E.E. Wolf, "Direct control of electron transfer to the surface-CO bond on a Pt/TiO2 catalytic diode," *Journal of the American Chemical Society* **2011**, 133, 16459-16467.

59 K. Hahn, "Atomic and molecular adsorption on Re(0001)," *Topics in Catalysis* **2014**, 57, 54-68.

60 J.A. Herron, S. Tonelli, M. Mavrikakis, "Atomic and molecular adsorption on Ru(0001)," *Surface Science* **2013**, 614, 64-74

61 D.C. Ford, Y. Xu, M. Mavrikakis, "Atomic and molecular adsorption on Pt(111)," *Surface Science* **2005**, 587, 159-174.

62 J.A. Herron, S. Tonelli, M. Mavrikakis, "Atomic and molecular adsorption on Pd(111)," *Surface Science* **2012**, 606, 1670-1679.

63 Y. Santiago-Rodriguez, J.A. Herron, M.C. Curet-Arana, M. Mavrikakis, "Atomic and molecular adsorption on Au(111)," *Surface Science* **2014**, 627, 57-69.

64 F. Che, S. Ha, J.-S. McEwen, "Elucidating the field influence on the energetics of the methane steam reforming reaction: A density functional theory study," *Applied Catalysis B: Environmental* **2016**, 195, 7-89.

65 F. Liu, T. Xue, C. Wu, S. Yang, "Coadsorption of CO and O over strained metal surfaces," *Chemical Physics Letters* **2019**, 722, 18-25.

66 Z.W. Ulissi, A.J. Medford, T. Bligaard, J.K. Norskov, "To address surface reaction network complexity using scaling relations machine learning and DFT calculations," *Nature Communications* **2017**, 8, 14621.

67 E.R. Kay, D.A. Leigh, F. Zerbetto, "Synthetic molecular motors and mechanical machines," *Angewandte Chemie International Edition* **2007**, 46, 72-191.

68 S. Erbas-Cakmak, D.A. Leight, C.T. McTernan, A.L. Nussbaumer, "Artificial Molecular Machines," Chemical Reviews 2015, 115, 10081-10206.

69 L. Zhang, V. Marcos, D.A. Leight, "Molecular machines with bio-inspired mechanisms," *PNAS* **2018**, 115(38), 9397.

70 V. Blanco, D.A. Leigh, V. Marcos, "Artificial switchable catalysts," *Chemical Society Reviews* **2015**, 44, 5341-5370.

71 J. Clayden, "No turning back for motorized molecules," *Nature* **2016**, 534, 187.

72 M.R. Wilson, J. Sola, A. Carlone, S.M. Goldup, N. Lebrasseur, D.A. Leigh, "An autonomous chemically fueled small-molecule motor," *Nature* **2016**, 534, 235.

73 C. Cheng, P.R. McGonigal, S.T. Schneebeli, H. Li, N.A. Vermeulen, C. Ke, J.F. Stoddart, "An artificial molecular pump," *Nature Nanotechnology*, **2015**, 10, 547.

74 I.M. Bennett, H.M. Vanegas Farfano, F. Bogani, A. Primak, P.A. Liddell, L. Otero, L. Sereno, J.J. Silber, A.L. Moore, T.A. Moore, D. Gust, "Active transport of Ca2+ by an artificial photosynthetic membrane". *Nature* **2002**, 420, 398–401.

75 E.R. Kay, D.A. Leigh, "Rise of the Molecular Machines," *Ang. Chem. Int. Ed.* **2015**, 54, 10080-10088.

76 V. Serreli, C.F. Lee, E.R. Kay, D.A. Leigh, "A molecular information ratchet," *Nature* **2007**, 445, 523-527.

77 R. D. Astumian, I. Derenyi, "Fluctuation driven transport and models of molecular motors and pumps," *Eur. Biophys. J.* **1998**, 27, 474-489.